

FORMATION AND DECAY OF THE INNER ELECTRON RADIATION BELT

Xinlin Li

**University of Colorado at Boulder, UCB 600
3665 Discovery Drive
Boulder, CO 80303-7820**

9 January 2017

Final Report

APPROVED FOR PUBLIC RELEASE; DISTRIBUTION IS UNLIMITED.



**AIR FORCE RESEARCH LABORATORY
Space Vehicles Directorate
3550 Aberdeen Ave SE
AIR FORCE MATERIEL COMMAND
KIRTLAND AIR FORCE BASE, NM 87117-5776**

DTIC COPY

NOTICE AND SIGNATURE PAGE

Using Government drawings, specifications, or other data included in this document for any purpose other than Government procurement does not in any way obligate the U.S. Government. The fact that the Government formulated or supplied the drawings, specifications, or other data does not license the holder or any other person or corporation; or convey any rights or permission to manufacture, use, or sell any patented invention that may relate to them.

This report was cleared for public release by the PRS OPSEC Office and is available to the general public, including foreign nationals. Copies may be obtained from the Defense Technical Information Center (DTIC) (<http://www.dtic.mil>).

AFRL-RV-PS-TR-2017-0019 HAS BEEN REVIEWED AND IS APPROVED FOR PUBLICATION IN ACCORDANCE WITH ASSIGNED DISTRIBUTION STATEMENT.

//SIGNED//

Dr. Richard Selesnick
Program Manager, AFRL/RVBXR

//SIGNED//

Dr. Thomas R. Caudill, Acting Chief
AFRL Battlespace Environment Division

This report is published in the interest of scientific and technical information exchange, and its publication does not constitute the Government's approval or disapproval of its ideas or findings.

REPORT DOCUMENTATION PAGE				Form Approved OMB No. 0704-0188	
Public reporting burden for this collection of information is estimated to average 1 hour per response, including the time for reviewing instructions, searching existing data sources, gathering and maintaining the data needed, and completing and reviewing this collection of information. Send comments regarding this burden estimate or any other aspect of this collection of information, including suggestions for reducing this burden to Department of Defense, Washington Headquarters Services, Directorate for Information Operations and Reports (0704-0188), 1215 Jefferson Davis Highway, Suite 1204, Arlington, VA 22202-4302. Respondents should be aware that notwithstanding any other provision of law, no person shall be subject to any penalty for failing to comply with a collection of information if it does not display a currently valid OMB control number. PLEASE DO NOT RETURN YOUR FORM TO THE ABOVE ADDRESS.					
1. REPORT DATE (DD-MM-YYYY) 09-01-2017		2. REPORT TYPE Final Report		3. DATES COVERED (From - To) 30 Jun 2014 to 30 Dec 2016	
4. TITLE AND SUBTITLE Formation and Decay of the Inner Electron Radiation Belt				5a. CONTRACT NUMBER FA9453-14-M-0256	
				5b. GRANT NUMBER	
				5c. PROGRAM ELEMENT NUMBER 69120J	
6. AUTHOR(S) Xinlin Li				5d. PROJECT NUMBER	
				5e. TASK NUMBER PPM00020550	
				5f. WORK UNIT NUMBER EF126454	
7. PERFORMING ORGANIZATION NAME(S) AND ADDRESS(ES) University of Colorado at Boulder, UCB 600 3665 Discovery Drive Boulder, CO 80303-7820				8. PERFORMING ORGANIZATION REPORT NUMBER	
9. SPONSORING / MONITORING AGENCY NAME(S) AND ADDRESS(ES) Air Force Research Laboratory Space Vehicles Directorate 3550 Aberdeen Avenue SE Kirtland AFB, NM 87117-5776				10. SPONSOR/MONITOR'S ACRONYM(S) AFRL/RVBXR	
				11. SPONSOR/MONITOR'S REPORT NUMBER(S) AFRL-RV-PS-TR-2017-0019	
12. DISTRIBUTION / AVAILABILITY STATEMENT Approved for public release; distribution is unlimited. (OPS-17-12877 dtd 19 Jan 2017)					
13. SUPPLEMENTARY NOTES					
14. ABSTRACT The distribution of radiation belt electrons and protons have been studied using data from the Van Allen Probes satellites and from The Colorado Student Space Weather Experiment. They have shown there is no steady population of trapped electrons above 1.6 MeV and described in detail the distribution of trapped protons. The results will aid in improving radiation environment specifications models for satellite design.					
15. SUBJECT TERMS radiation belt, electrons, protons					
16. SECURITY CLASSIFICATION OF:			17. LIMITATION OF ABSTRACT	18. NUMBER OF PAGES	19a. NAME OF RESPONSIBLE PERSON
a. REPORT	b. ABSTRACT	c. THIS PAGE			Dr. Richard Selesnick
Unclassified	Unclassified	Unclassified	Unlimited	10	19b. TELEPHONE NUMBER (include area code)

This page is intentionally left blank.

Table of Contents

1. INTRODUCTION	1
2. BACKGROUND	1
3. METHODS, ASSUMPTIONS, AND PROCEDURES	1
4. RESULTS AND DISCUSSION.....	2
5. CONCLUSIONS.....	2
APPENDIX A - Upper limit on the inner radiation belt MeV electron intensity.....	3
APPENDIX B - Observations of the inner radiation belt: CRAND and trapped solar protons.....	17
APPENDIX C - Inward diffusion and loss of radiation belt protons	29

This page is intentionally left blank.

1. INTRODUCTION

The inner radiation belt presents a hazard to satellites in low-Earth orbit (LEO) and geosynchronous-transfer orbit that can be damaged by the intense charged-particle environment. Protons are the prominent hazard, often causing single event upsets in onboard electronics, but the less intense electrons cause deep dielectric charging that is a separate concern. It is therefore desirable to describe the distribution of both particle populations and to understand their sources and losses for prediction of future variability.

2. BACKGROUND

This work was part of a NASA-funded project at AFRL to study formation and decay of the inner electron radiation belt. These basic processes have been poorly understood and the recent availability of new electron measurements from the Van Allen Probes and other satellites has prompted such a re-evaluation. The University of Colorado collaborators, led by Professor Xinlin Li, contributed data and analysis from their Colorado Student Space Weather Experiment (CSSWE), a CubeSat satellite designed, built, and operated by them that carries electron and proton detectors in LEO. The University of Colorado also provided expert knowledge of the Relativistic Electron Proton Telescope (REPT) particle detectors on the NASA/Van Allen Probes that were designed, built, and operated at the University's Laboratory for Atmospheric and Space Physics (LASP).

3. METHODS, ASSUMPTIONS, AND PROCEDURES

A primary goal was to determine whether there is a significant stable population of inner belt electrons with energies above 1 MeV, as has long been assumed. To this end, we performed a detailed evaluation of data from the REPT instruments on Van Allen Probes. We made use of the pulse-height-analyzed (PHA) data that are not included in the routine (Level 2) data products. These enabled a careful evaluation of high-energy (>100 MeV) proton contamination.

We also made use of electron data from the Relativistic Electron Proton Telescope integrated little experiment (REPTile) instrument on the low-altitude CSSWE satellite. We evaluated electron intensity in the drift loss cone (DLC), to determine as a function of energy the longitude that is expected as a result of atmospheric scattering.

Substantial contamination of the Van Allen Probes REPT by the inner belt protons was found while conducting the electron data analysis. It was then a straightforward task to subtract this background from the proton data and accurately evaluate the proton intensity and distribution as a function of energy, equatorial pitch angle, and magnetic L-shell.

4. RESULTS AND DISCUSSION

We found that both the electron and proton measurements from REPT were subject to substantial contamination in the inner belt. After subtracting this background we found no evidence of any inner-belt electron population with energy greater than 1.6 MeV. Based on these findings we determined an upper limit on the inner belt high-energy electron intensity that was lower than previously accepted values for the trapped electron intensity, suggesting that earlier measurements could have been similarly contaminated. By evaluating electron intensity in the drift loss cone (DLC), increasing with longitude as expected on the basis of atmospheric scattering, results from CSSWE confirmed a population of low-energy (<1 MeV) inner-belt electrons. However, they showed no such scattered population of DLC electrons for higher energies. This provided independent confirmation of the conclusion from REPT data that any stable population of trapped high-energy inner-belt electrons has significantly lower intensity than has been accepted previously. This work was published in the Journal of Geophysical Research (JGR) [Appendix A].

The REPT proton data analysis results showed that a significant proton loss occurred during large magnetic storms in 2015, that a steady increase in proton intensity near $L = 2$ results from inward diffusion of trapped solar protons, and that a deficiency of trapped protons with kinetic energy above 50 MeV near $L = 1.5$, relative to theoretical expectations, indicates a previously unknown steady loss process. These results were published in two JGR research articles [Appendix B and Appendix C].

5. CONCLUSIONS

This work has contributed significantly to our knowledge of the inner radiation belt. It has shown there is no steady population of trapped electrons above 1.6 MeV and described in detail the distribution of trapped protons. The results will aid in improving radiation environment specifications models for satellite design.



RESEARCH ARTICLE

10.1002/2014JA020777

Special Section:

New perspectives on Earth's radiation belt regions from the prime mission of the Van Allen Probes

Key Points:

- Quantified upper limit of MeV electrons in the inner belt
- Actual MeV electron intensity likely much lower than the upper limit
- More detailed understanding of relativistic electrons in the magnetosphere

Correspondence to:

X. Li,
lix@lasp.colorado.edu

Citation:

Li, X., R. S. Selesnick, D. N. Baker, A. N. Jaynes, S. G. Kanekal, Q. Schiller, L. Blum, J. Fennell, and J. B. Blake (2015), Upper limit on the inner radiation belt MeV electron intensity, *J. Geophys. Res. Space Physics*, 120, 1215–1228, doi:10.1002/2014JA020777.

Received 29 OCT 2014

Accepted 14 JAN 2015

Accepted article online 18 JAN 2015

Published online 24 FEB 2015

This is an open access article under the terms of the Creative Commons Attribution-NonCommercial-NoDerivs License, which permits use and distribution in any medium, provided the original work is properly cited, the use is non-commercial and no modifications or adaptations are made.

Upper limit on the inner radiation belt MeV electron intensity

X. Li^{1,2}, R. S. Selesnick³, D. N. Baker¹, A. N. Jaynes¹, S. G. Kanekal⁴, Q. Schiller^{1,2}, L. Blum^{1,2,5}, J. Fennell⁶, and J. B. Blake⁶

¹Laboratory for Atmospheric and Space Physics, University of Colorado Boulder, Boulder, Colorado, USA, ²Department of Aerospace Engineering Sciences, University of Colorado Boulder, Boulder, Colorado, USA, ³Space Vehicles Directorate, Air Force Research Laboratory, Kirtland AFB, New Mexico, USA, ⁴NASA/Goddard Space Flight Center, Greenbelt, Maryland, USA, ⁵Now at Space Sciences Laboratory, University of California, Berkeley, California, USA, ⁶Space Science Applications Laboratory, Aerospace Corporation, El Segundo, California, USA

Abstract No instruments in the inner radiation belt are immune from the unforgiving penetration of the highly energetic protons (tens of MeV to GeV). The inner belt proton flux level, however, is relatively stable; thus, for any given instrument, the proton contamination often leads to a certain background noise. Measurements from the Relativistic Electron and Proton Telescope integrated little experiment on board Colorado Student Space Weather Experiment CubeSat, in a low Earth orbit, clearly demonstrate that there exist sub-MeV electrons in the inner belt because their flux level is orders of magnitude higher than the background, while higher-energy electron (>1.6 MeV) measurements cannot be distinguished from the background. Detailed analysis of high-quality measurements from the Relativistic Electron and Proton Telescope on board Van Allen Probes, in a geo-transfer-like orbit, provides, for the first time, quantified upper limits on MeV electron fluxes in various energy ranges in the inner belt. These upper limits are rather different from flux levels in the AE8 and AE9 models, which were developed based on older data sources. For 1.7, 2.5, and 3.3 MeV electrons, the upper limits are about 1 order of magnitude lower than predicted model fluxes. The implication of this difference is profound in that unless there are extreme solar wind conditions, which have not happened yet since the launch of Van Allen Probes, significant enhancements of MeV electrons do not occur in the inner belt even though such enhancements are commonly seen in the outer belt.

1. Introduction

Earth's radiation belts are divided into three regions: the inner belt, centered near 1.5 Earth radii (R_E) from the center of the Earth when measured in the equatorial plane; the outer belt, which is most intense between 4 and 5 R_E for relativistic electrons (>500 keV); and the "slot" region, centered near 2.5 R_E , which appears to separate the two radiation belts during quiet times but can be filled with relativistic electrons during active times. The outer belt electrons are constantly decaying and episodically reforming, on a time scale of hours to days, and each reformed belt may have a different center location and intensity [Li and Temerin, 2001]. In contrast, Earth's inner radiation belt is much more stable. It contains an intense and stable population of geomagnetically trapped protons with kinetic energies up to ~1 GeV, formed by cosmic ray albedo neutron decay (CRAND) and solar proton trapping [Selesnick et al., 2014]. The CRAND process also produces electrons, with kinetic energies primarily below 800 keV but is thought not to be a significant source of trapped electrons [Lenchek et al., 1961]. This conclusion is supported by the unsteady nature of inner belt electron intensity observed at these lower energies, with rapid (~1 day) injections followed by slow decay [Rosen and Sanders, 1971]. Exponential decay timescales (e-folding times) are ~100 days [Selesnick, 2012]. Injections occur most frequently at the lower energies (<600 keV), typically several times per year [Zhao and Li, 2013b], but only occasionally for higher kinetic energies, $E \geq 1$ MeV [Baker et al., 2007; Zhao and Li, 2013a]. Intense high-energy injections occurred in March 1991 [Blake et al., 1992], associated with an unusually strong interplanetary shock [Li et al., 1993], and October 2003 [Baker et al., 2004], that produced an extreme magnetic storm ($Dst \lesssim -400$ nT) and for which the injection mechanisms are still debated [Horne et al., 2005; Kress et al., 2007; Li et al., 2009]. The trapped multiple-MeV electrons with decaying intensity were subsequently observed for years in each case [e.g., Looper et al., 1994].

Rare injections of high-energy electrons into the inner belt undoubtedly occur. However, some measurements, which are subject to contamination from inner belt protons, might have suggested a steady

population of high-energy inner-belt-trapped electrons. The relative stability of the inner belt has been attributed to continuous replenishment by inward diffusion of electrons from the outer radiation belt [Lyons and Thorne, 1973]. Although the viability of such a source has been questioned [Kim and Shprits, 2012], the reality of a stable-trapped electron population typically has not. In fact, the widely applied AE8 and AE9 empirical radiation belt models both specify substantial populations of inner belt high-energy electrons without any time dependence [Vette, 1991; Ginet et al., 2013].

A strong resemblance between the stable inner belt proton distribution and the supposed electron distribution, in both space and time, is a clue that they may, in fact, be one and the same. The reliability of proton measurements is well documented [Selesnick et al., 2014] but not so for MeV electrons. Therefore, the possibility should be carefully considered that other measurements of a stable inner belt electron intensity for $E \geq 1$ MeV are erroneous, resulting from contamination by protons.

In this paper, data from the Relativistic Electron Proton Telescope (REPT) [Baker et al., 2012] on each of the two Van Allen Probes satellites [Mauk et al., 2012; Kessel et al., 2012] and the Relativistic Electron Proton Telescope integrated little experiment (REPTile) on board Colorado Student Space Weather Experiment (CSSWE) [Li et al., 2012, 2013a] are analyzed for possible detection of inner belt high-energy electrons. REPT is part of the Radiation Belt Storm Probes-Energetic Particle, Composition, and Thermal Plasma (RBSP-ECT) suite [Spence et al., 2013], which consists of three sets of measurements: Helium, Oxygen, Proton, and Electron (HOPE) [Funstein et al., 2013] covering 10 eV to 50 keV; Magnetic Electron Ion Spectrometer (MagEIS) [Blake et al., 2013] covering 37 keV to 4 MeV; and REPT covering 1.6 MeV to 10 MeV electrons with each sensor designed to reduce or remove backgrounds expected from protons in the inner zone.

2. REPT and REPTile Data

REPT contains a stack of nine aligned Si solid state detectors that each measures energy deposition from charged particles. In combination they provide an accurate determination of incident kinetic energy for particles that enter through the front collimator (with a 32° field of view) and stop in one of the detectors and integral energy determinations for those particles that fully penetrate the stack. Discrimination between species and energy of protons and electrons is nominally achieved from a set of logic conditions [Baker et al., 2012]. However, for the analysis presented in the paper, the logic conditions are not used but replaced by equation (1) to be described in section 3.

A subset of the REPT data are available as pulse height analyzer (PHA) events with fast time resolution (12 ms between events) that specify the energy deposits measured simultaneously in every detector. Each event ideally represents a single charged particle measurement. Together they form a detailed data set for differential high-energy electron and proton measurements and are used in this study. A data analysis method for discerning proton deposits from PHA data has been described previously [Selesnick et al., 2014] and is here adapted for electron data.

REPTile is a simplified and miniaturized version of REPT and has a robust design verified with Geometry and Tracking 4 (Geant4) simulations [Agostinelli et al., 2003; Schiller and Mahendrakumar, 2010; Li et al., 2013b]. Since CSSWE is in a highly inclined (65°) low Earth orbit, 480 km \times 780 km, CSSWE traverses the radiation belts 4 times in each orbit (~ 1.5 h), providing a global view of their spatial structure [Li et al., 2013b]. Figure 1 shows energetic electron and proton fluxes in REPTile's first two energy channels plotted versus geographic longitude and latitude for a 4 day interval, 10–14 January 2013. The electrons are seen in a two-belt structure, with inner belt only seen above the South Atlantic Anomaly (SAA) region, where the Earth's magnetic field is weak. The outer belt lower energy electrons, 0.58–1.63 MeV, penetrate into the lower latitude or lower L , which represents the geocentric distance in R_E at the equator of the shell if the Earth's magnetic field is approximated as a dipole, and some of them seem to merge with the inner belt, visible in the south of SAA region. The higher-energy electrons, 1.63–3.8 MeV, seem to be clearly separated from the inner belt. There are no solar energetic particle events during this period nor are any energetic protons detected in the outer belt. Energetic protons are thus detectable only when above the SAA region. A few points are worth noting here: (1) the intensity of 9–18 MeV protons is lower than 18–30 MeV protons, which is consistent with previous finding [Selesnick et al., 2007], due to the faster loss of lower energy protons created by CRAND; (2) the lower energy electrons are in a much wider region around the SAA, and their flux is orders of magnitude higher than the proton flux in the SAA, demonstrating an abundance

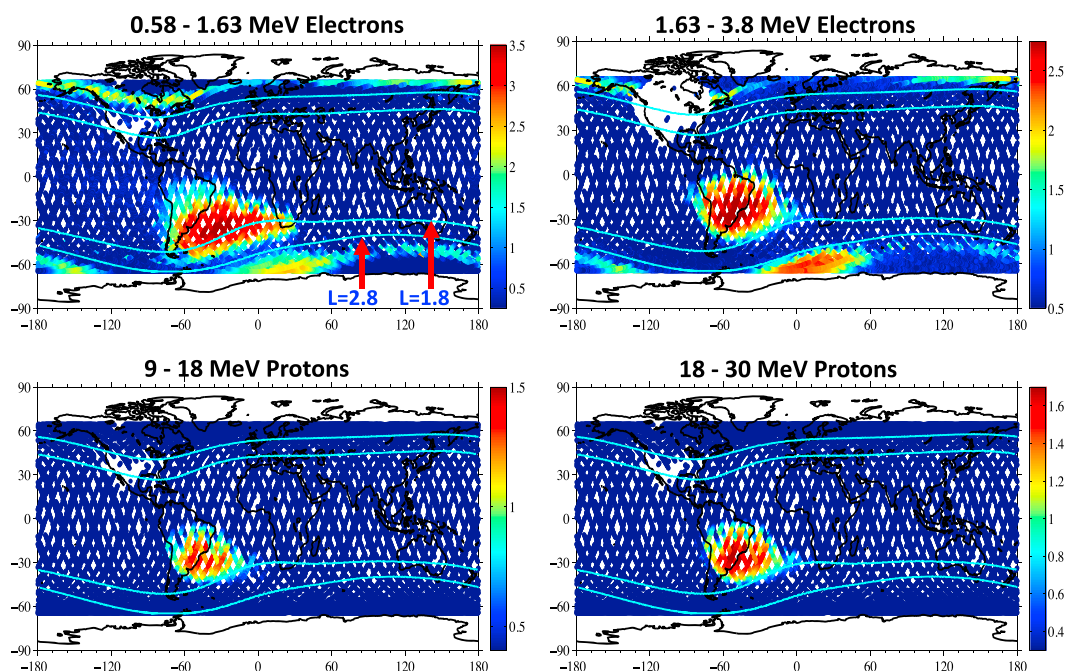


Figure 1. Mercator map of electron and proton fluxes from the first two energy channels of REPTile during 10–14 January 2013.

of such low-energy electrons in the inner belt as well as in the slot region; (3) the higher-energy electrons show a similar shape and flux level in the SAA as the protons, suggesting that the proton contamination can be significant for the higher-energy channel. Such similarity remains the same for some more active period, such as in the middle of October 2012 [Li *et al.*, 2013b], while the outer belt electrons can be much different. Thus, we should look at these issues more carefully.

Figure 2 shows measurements of these two channels taken in the Southern Hemisphere (blue) and Northern Hemisphere (red) as a function of the magnetic longitude for a longer period, 4–14 January 2013, for better statistics. As the electrons drift eastward, they are subjected to pitch angle scattering. Electrons that can be measured by REPTile in the north will precipitate into atmosphere in the SAA because their corresponding mirroring points would be below 100 km altitude.

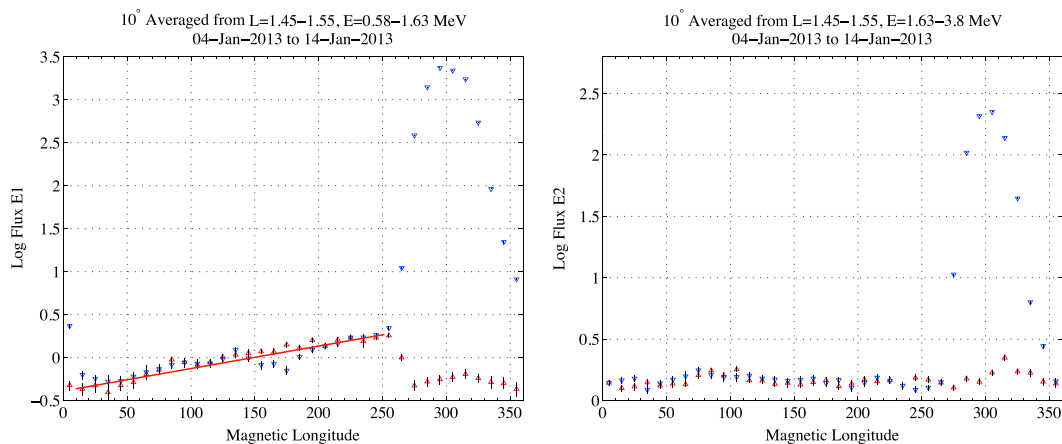
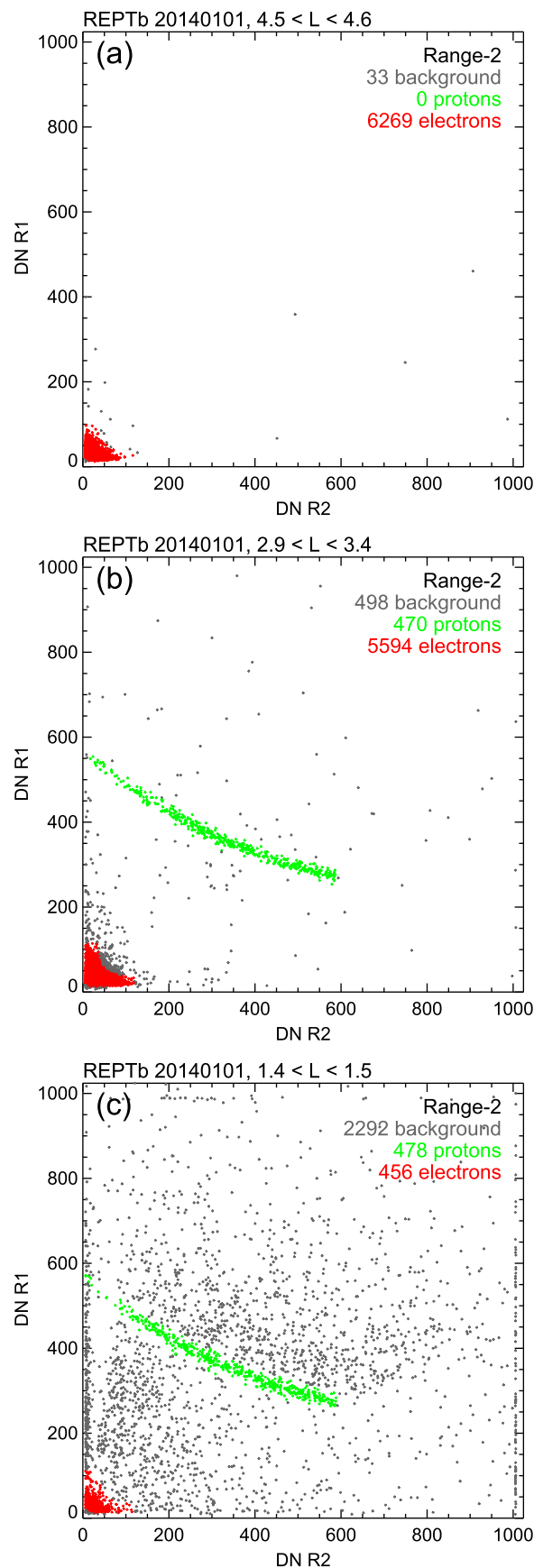


Figure 2. REPTile measurements around $L = 1.7$ in the Southern Hemisphere (blue) and Northern Hemisphere (red) versus magnetic longitude for the time period of 4–14 January 2013. The red line on the left figure guides the slope, which suggests a weak pitch angle diffusion as the electrons drift toward the South Atlantic Anomaly region, $>250^\circ$.



In the drift loss cone (DLC, longitudes $< 250^\circ$) the lower energy E1 channel measurements show increasing flux (red line) as quasi-trapped electrons drift eastward. This is caused by large-angle, nondiffusive, pitch angle scattering of stably trapped electrons from Coulomb collisions with atmospheric neutral atoms, plasma ions, and free electrons [Selesnick, 2012]. Flux increases eastward during the time, ~ 1 h, required to drift through the DLC before reaching the SAA (longitudes $> 250^\circ$), where electrons are lost in the dense atmosphere and where higher fluxes of stably trapped electrons are seen in the figure. Similar flux variations in outer belt electron data are caused by weak pitch angle diffusion from scattering by plasma waves [Selesnick, 2006; Tu *et al.*, 2010]. Similar variations should also be expected for the higher-energy channel from REPTile in the inner belt if it also measures quasi-trapped electrons in the DLC and stably trapped electrons in the SAA. However, the E2 channel data in Figure 2 do not show such a pattern, casting doubt on the existence of such high-energy electrons (> 1.6 MeV) in the inner belt.

The question is how to quantify the high-energy electron flux in the inner belt or at least find an upper limit. This will be the main focus of the following based on REPT measurements.

3. Particle Identification in REPT Measurements

Examples of PHA data taken by REPT-B (on the RBSP-B spacecraft) during a single day (1 January 2014) are shown in Figure 3. Data numbers (DN)

Figure 3. REPT pulse height data for Range-2 events from a single day, 1 January 2014. The DN values from R1 and R2 are proportional to energy deposited in those detectors. Three L shell ranges represent (a) the outer belt electron peak, (b) the inner edge of outer belt electrons and outer edge of inner belt protons, and (c) the inner belt proton peak. Preliminary event identification, as described in the text, is indicated by color for protons (green), electrons (red), and background (gray). The number of events of each type in each L range is indicated.

proportional to energy loss, Δ , in a given detector, where Δ in MeV is $\sim \text{DN}/38$ (the exact value varies between detectors and spacecraft). Figure 3 shows DN from the front detector (R1) versus DN from the second detector (R2), for so-called Range 2 events (events in which only the first two detectors were triggered and both had nonzero DN). Data are also separated by L : (a) $4.5 < L < 4.6$, near the outer zone electron peak; (b) $2.9 < L < 3.4$, near the inner edge of the electron outer zone and the outer edge of the proton inner zone; and (c) $1.4 < L < 1.5$, near the inner zone proton peak.

In Figure 3, events are nominally identified as protons (green), electrons (red), or background (gray). Similar identification is made for events with higher ranges, for which data from more detectors are available. To be considered a valid Range n proton or electron event there must be a high probability that the particle was in the REPT field of view (FOV), entered the detector stack at R1, and stopped in detector R_n . Low probability, or background, events can result from high-energy protons that were outside the FOV, or perhaps from electrons in the FOV that scattered out of the detector stack. The valid Range 2 events of Figure 3 have kinetic energies ~ 20 to 30 MeV for protons and ~ 1.5 to 3 MeV for electrons before passing through the 2 mm Be window (at the front of the detector stack) and R1 and finally stopping in R2.

The probability density function (PDF) for energy loss Δ in a path length x from an incident energy E is called the straggling function, $f(\Delta, E, x)$ [Bichsel, 1988]. The probability of a valid Range n event is given by the following product:

$$f_{n-1}(E, \theta) = \prod_{i=1}^{n-1} f(\Delta_i, E - E_{i-1}, x_i \sec \theta) \quad (1)$$

where the straggling function f is the probability density for measured energy loss Δ_i in detector i of thickness x_i with incident angle θ . The incident energy E (after going through the Be window) at R1 is reduced by the total energy loss up to detector i :

$$E_{i-1} = \sum_{j=1}^{i-1} \Delta_j \quad (2)$$

The straggling function $f(\Delta, E, x \sec \theta)$ may also be viewed as the distribution of energy deposits Δ that would be measured in a detector of thickness x from many particles all with the same incident energy E and angle θ . It represents the probability of a particular Δ given E and θ , or, equivalently, of a particular E and θ given Δ . Since the energy deposits Δ_i measured by consecutive detectors in REPT are independent random processes, the product of probabilities, f_{n-1} , in equation (1) is the probability of a particular E and θ given a set of measured Δ_i . This probability depends on the assumed type of incident particle, proton, or electron, because the straggling functions are different for each. Therefore, by evaluating f_{n-1} separately for each particle type, the probabilities that a given event corresponded to an incident proton or electron are determined. If one of the probabilities is above a certain threshold, e.g., $f_{\min} \sim 10^{-3}$ in the Range 2 event for either protons or electrons, then it is counted as a particle of that type. If neither of the probabilities are above the threshold, then it is a background event. (It never occurs that both probabilities are above the threshold because the proton and electron regions shown in Figure 3 do not overlap.)

For protons, accurate approximations are available for the straggling function [Selesnick et al., 2014] and f_{n-1} is evaluated at the incident energy for a particle stopping in detector n , $E = E_n$, and for the mean incident angle $\bar{\theta}$ over the distribution $f_{n-1}(E_n, \theta)$.

Electrons can scatter significantly in the detector stack, and the incident angle at each detector is likely to vary. Evaluation of f_{n-1} is therefore more complex. However, a simplified approach was adopted for the task of electron identification by assuming the following: incident angle $\theta = 0$ at each detector, and the straggling function f is the universal Landau distribution [Schorr, 1974], which is accurate in the limiting case of thin detectors. Because the method is used only for identification of candidate electron events, the validity of this simplified approach is determined by its accuracy in cases where nearly all events are known to be electrons.

For the outer zone region represented in Figure 3a, as expected, no valid proton events are identified and virtually all of the Range 2 events are identified as valid electrons. The small fraction of background events may result from cosmic rays.

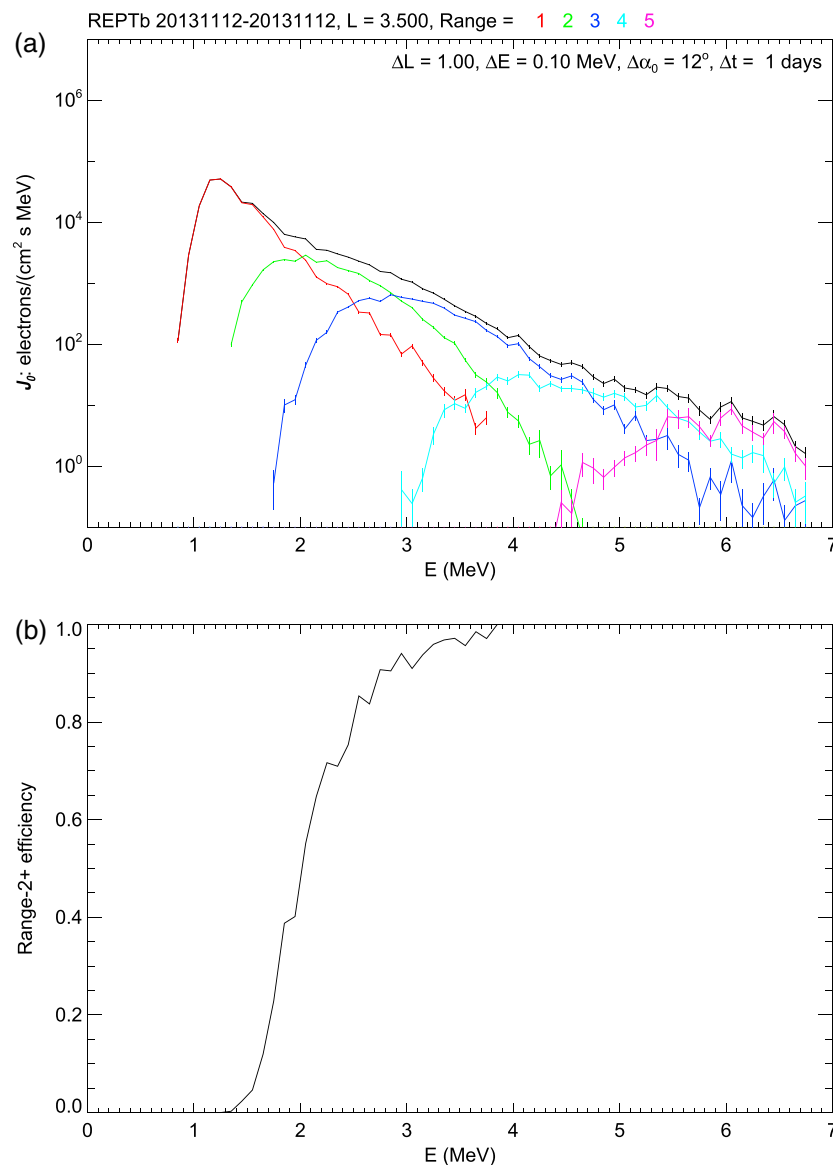


Figure 4. (a) Average omnidirectional equatorial electron energy spectrum (black) from REPT PHA data for $3 < L < 4$ during 11 November 2013. Color-coded contributions from each Range 1 through 5 are also shown. Bin widths used in the data analysis are listed. (b) Derived electron detection efficiency excluding the Range 1 data.

For the medium L region represented in Figure 3b, both inner zone protons and outer zone electrons are identified. The background is higher, caused by protons outside the FOV and perhaps also by electrons that were not properly identified. However, as in Figure 3a, most of the candidate electron events were identified as valid, justifying the simplified approach described above. Very few proton events, or background events of indeterminate origin, were incorrectly identified as electrons, which have a very different energy deposit pattern. The low number of background events, relative to the number of valid electron events, leaves little doubt that most of the events are properly identified in this case.

For the inner zone, Figure 3c, valid proton and electron events are identified, but most of the PHA events are background caused by intense high-energy protons. These protons can penetrate the thick shielding, outside the FOV, that stops lower energy protons and electrons. Some background events are in close proximity, by DN value, to the identified electron events. Therefore, their classification as electrons is now dubious and should be confirmed or refuted by other means, as discussed in detail below.

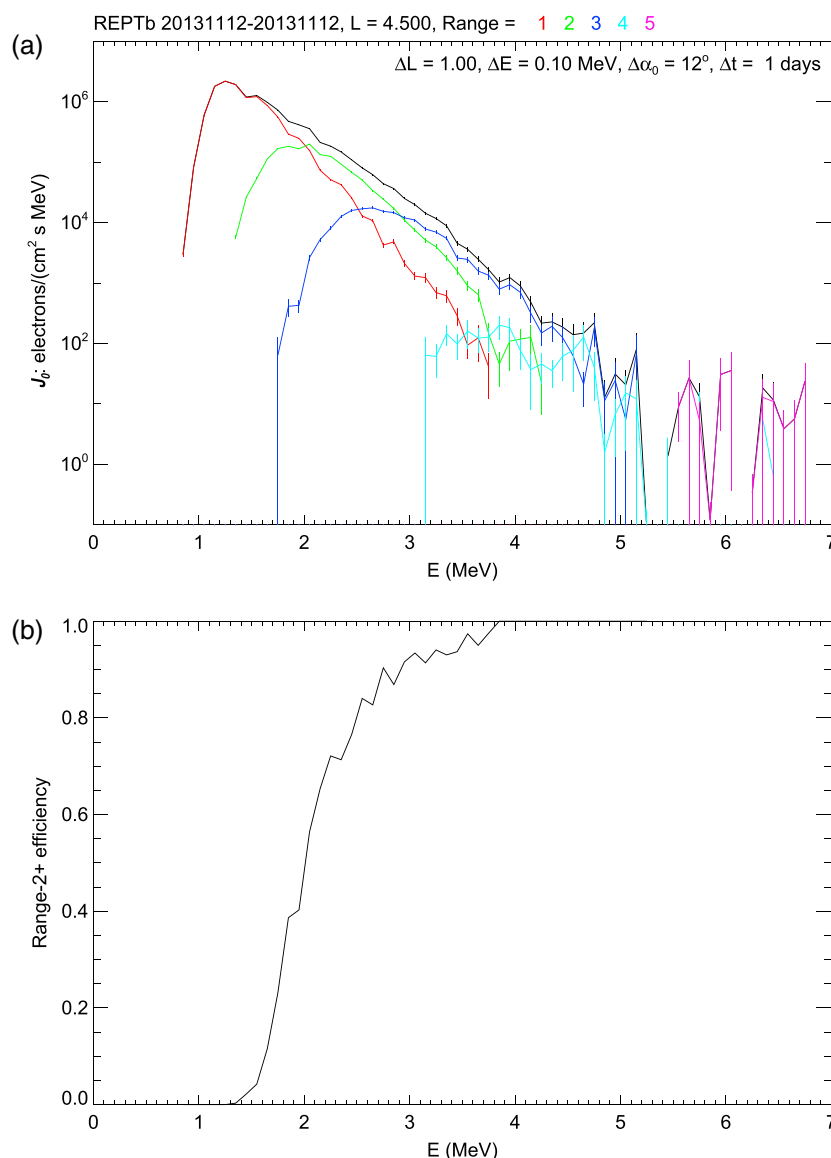


Figure 5. Similar to Figure 4 but for $4 < L < 5$.

4. Energy Spectra of REPT Measurements

After valid PHA events have been identified, computation of particle intensity as a function of energy and pitch angle is straightforward for protons [Selesnick *et al.*, 2014], because the detection efficiency in the FOV is near unity. For electrons, scattering can reduce the detection efficiency. However, the REPT design minimizes scattering effects [Baker *et al.*, 2012] and the same method for computing particle intensity is adapted here for electrons.

Outer zone electron omnidirectional differential energy spectra are shown in Figures 4a and 5a (black traces), averaged over the ranges $3 < L < 4$ and $4 < L < 5$, respectively. They are from REPT-A and REPT-B data combined and averaged over a 1 day interval (12 November 2013). Also shown are separate contributions to the total from the individual ranges $n = 1$ to 5 (colored traces). Range 1 events, for which only detector R1 is triggered, are useful in the outer zone, where it is safe to assume that all events are due to electrons. They provide a lower energy threshold than the Range 2 or greater events that are represented in the nominal energy ranges of REPT [Baker *et al.*, 2012].

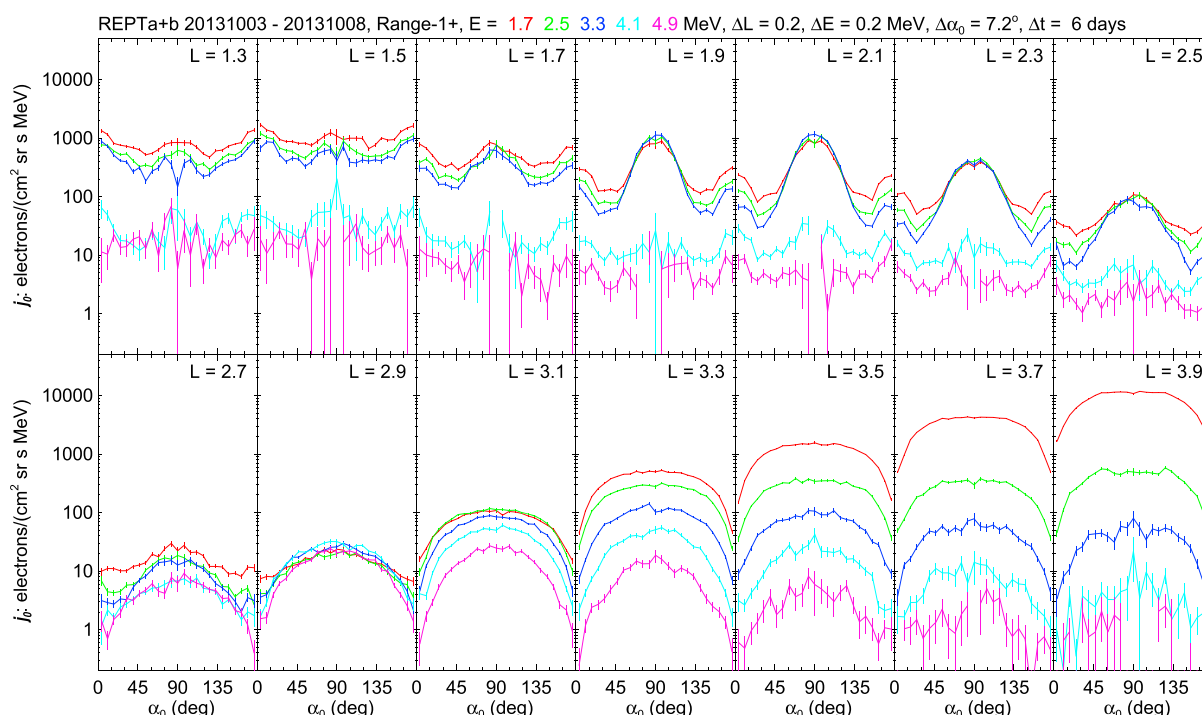


Figure 6. Average equatorial pitch angle distributions derived from REPT PHA events identified tentatively as electrons in Ranges 1 through 5, for separate L values from 1.3 to 3.9, during 3 through 8 October 2013. Electron energies are color coded. Bin widths used in the data analysis are listed.

For the inner zone, Range 1 data are less useful for electron measurements because of the intense high-energy proton population, which can penetrate shielding outside the FOV and trigger R1 but not R2 and beyond. However, the ratio of outer zone spectra calculated with and without the Range 1 data (red line in Figures 4a and 5a) provides an efficiency factor for correcting intensities calculated from Range 2 and above, extending their utility to lower energies. This efficiency factor is shown in Figures 4b and 5b. Despite the harder energy spectrum at lower L ($= 3.5$), the efficiency factors from the two L ranges (3.5 and 4.5) are in close agreement. They extend the useful energies of the Range 2 electron data down to ~ 1.5 MeV in the outer zone. However, Range 2 and beyond data are still to be tested in the inner zone, as to be described in the next section.

5. Pitch Angle Distributions

Van Allen Probes satellites are oriented such that the spin axis is roughly in the sunward direction, with a spin period of ~ 12 s. Directional differential intensity, from PHA events nominally identified as electrons, is shown in the form of equatorial pitch angle distributions (PADs) at selected L and E values in Figures 6 and 7. Data are from REPT-A and REPT-B data combined and averaged over a 6 day interval (3–8 October 2013). Figure 6 includes data from Ranges 1 to 5 events; Figure 7 includes only Ranges 2 to 5 events but uses the efficiency from Figure 5b (Figure 4b gives essentially the same efficiency) as a correction factor for the lower energies. For the lower energies, $E = 1.7, 2.5$, and 3.3 MeV, Figure 6 includes the Range 1 data but Figure 7 does not. The smaller number of events used in Figure 7 is combined with a smaller efficiency factor to determine electron intensities, which should thereby agree with those of Figure 6.

For the outer zone, $L \geq 3$, Figures 6 and 7 are indeed in close agreement as expected from data dominated by electrons. Distributions are characteristic of trapped electrons, with broad maxima near equatorial pitch angle $\alpha_0 = 90^\circ$ and minima associated with the loss cones at $\alpha_0 = 0$ and 180° (loss cones are not fully resolved because of the 32° FOV).

For the inner zone, $L \leq 3$, there is strong disagreement between Figures 6 and 7. Distributions narrowly peaked at $\alpha_0 = 90^\circ$ from the Range 1 data ($1.7 \leq L \leq 2.5$ in Figure 6) result from high-energy protons with degraded energy deposits in R1 (likely from skimming the edge of R1 and masquerading as electrons),

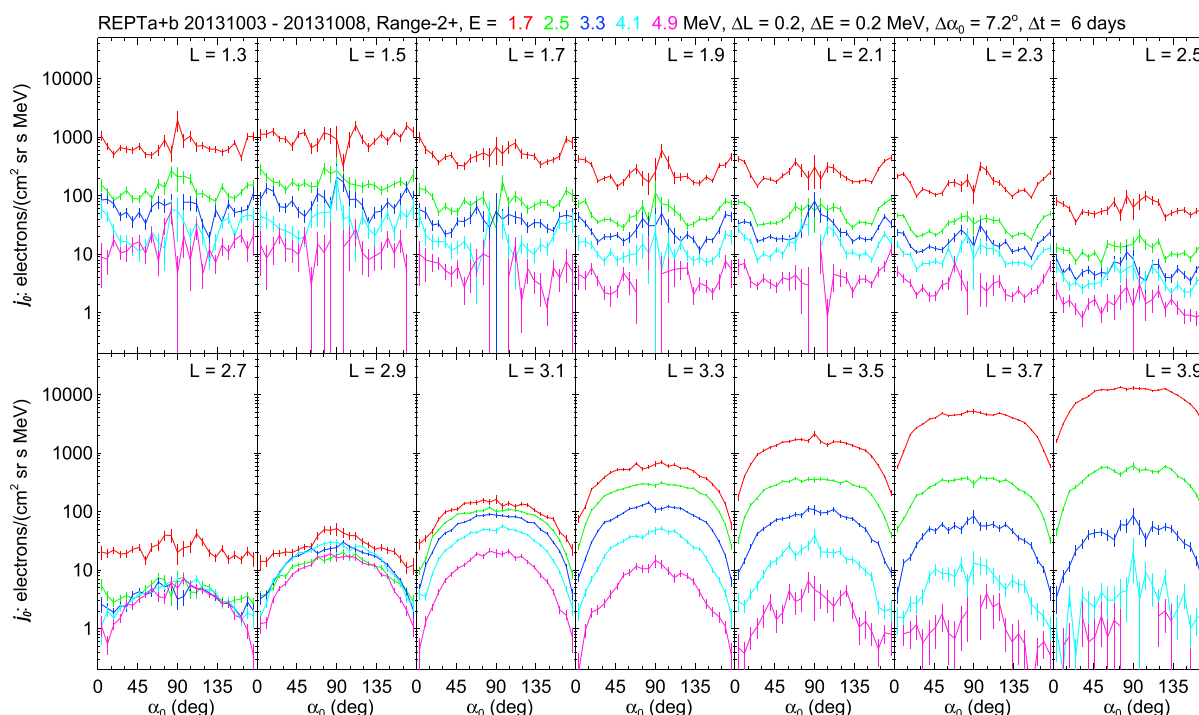


Figure 7. Similar to Figure 6 but from PHA data in Ranges 2 through 5 only.

as confirmed by comparison with reliable measurement of the proton pitch angle distributions [Selesnick *et al.*, 2014]. Clearly, the Range 1 data should not be used for inner zone electron measurements. In fact, all REPT data that are publicly available do not include any Range 1 data. Here the Range 1 data are shown in comparison with Range 2 data as a test of both data types.

The results from excluding Range 1 data (Figure 7) do not show such clear inner zone proton contamination, but neither are the distributions characteristic of trapped electrons. Within statistical uncertainties, they are essentially isotropic for $L \leq 2.7$. Loss cones widen with decreasing L , with widths $\sim 60^\circ$ at the lowest L values [Selesnick *et al.*, 2014]. That prominent loss cones are not evident in the inner zone pitch angle distributions suggests that the measured electron intensities there are results of contamination. The likely explanation is that the intensity of any high-energy electrons that may be present is dominated by the background caused by inner zone protons (Figure 3c). The background events can result from relativistic (≥ 500 MeV) protons, that leave low-energy deposits thus mimicking electrons, or from degraded energy deposits of lower energy protons. In either case, the proton energies are high enough (≥ 100 MeV) to penetrate the shielding around REPT and enter the detector stack at large angles to the telescope axis (rare nuclear scattering events in the detector stack may also contribute to the background). The pitch angle distributions therefore appear isotropic even though the protons themselves are in trapped distributions [Selesnick *et al.*, 2014].

6. Time Dependence

Omnidirectional differential intensity, from Range 2 and greater PHA events nominally identified as electrons, is shown as a function of L and time in Figure 8, for (a) $E = 2.1$ MeV and (b) $E = 4.9$ MeV. Data are from REPT-A and REPT-B data combined and averaged over 2 day intervals from October 2013 to March 2014.

For $L \geq 2.6$ there are intensity variations at both energies that are characteristic of outer zone electrons. Near the start of the interval, higher-energy electrons near $L = 3$ are unusually intense (Figure 8b), as seen also in the PADs (Figure 6 or 7), but decay with time.

For $L \leq 2.6$ the inner zone intensities are stable over time for both energies, apart from statistical fluctuations. It has already been seen that the inner zone data are dominated by proton background at

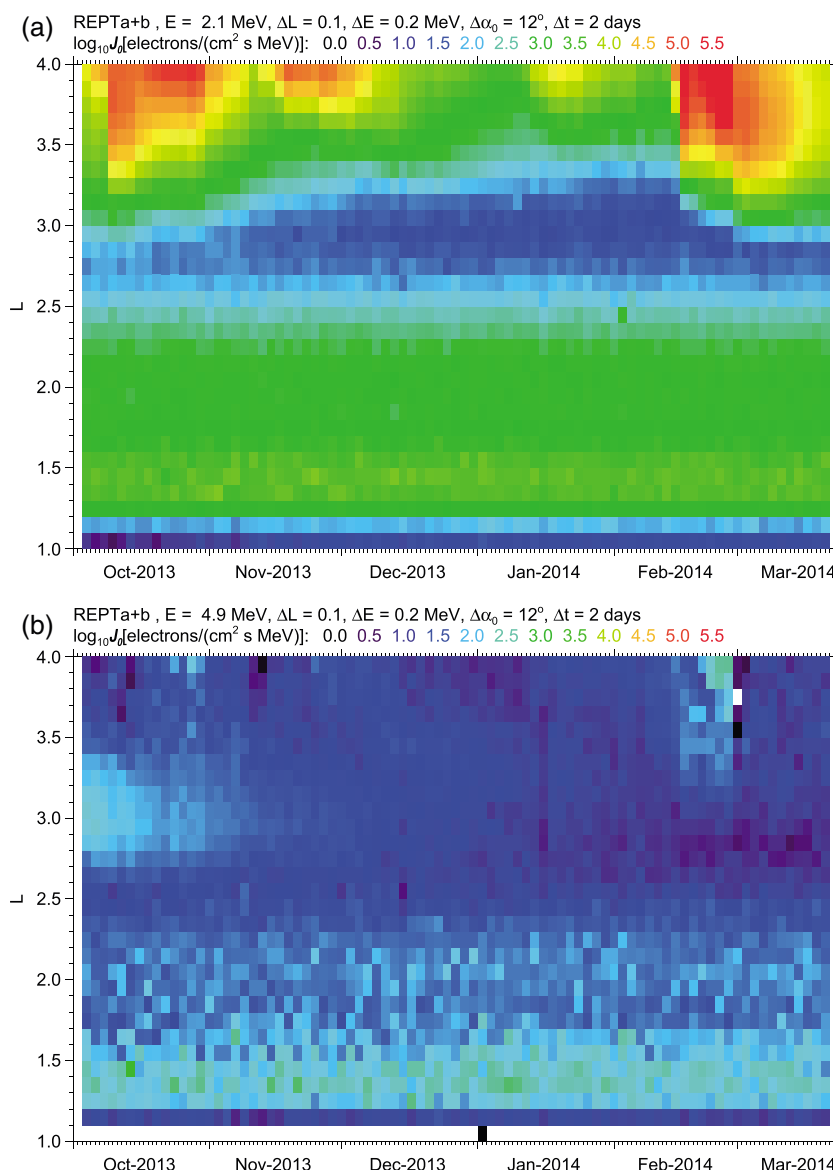


Figure 8. Color-coded omnidirectional equatorial intensity of REPT PHA events identified tentatively as electrons versus L and time for electron energies of (a) 2.1 MeV and (b) 4.9 MeV. Bin widths used in the data analysis are listed.

the start of the interval. Since there were no clear injections of high-energy electrons, the same conclusion applies throughout the interval.

7. Upper Limits

Omnidirectional differential intensity, from Range 2 and greater PHA events nominally identified as electrons, is shown as a function of L for selected energies in Figure 9. Data are from REPT-A and REPT-B data combined and averaged over a 6 day interval (3–8 October 2013), as in Figure 7. Inner zone regions where pitch angle distributions show that the data are in fact dominated by proton background are indicated (dashed lines in the figure). They vary from $L < 2.8$ for $E = 1.7$ MeV to $L < 2.5$ for $E = 4.9$ MeV, the higher energies being more reliable because proton background is lower when more detectors are triggered. The conclusion that the data are dominated by proton background is supported by the strong resemblance of the L distributions to those observed for trapped protons during the same time interval [Selesnick *et al.*, 2014]. In these inner zone regions the measured intensities should be considered upper limits on the actual trapped electron intensity.

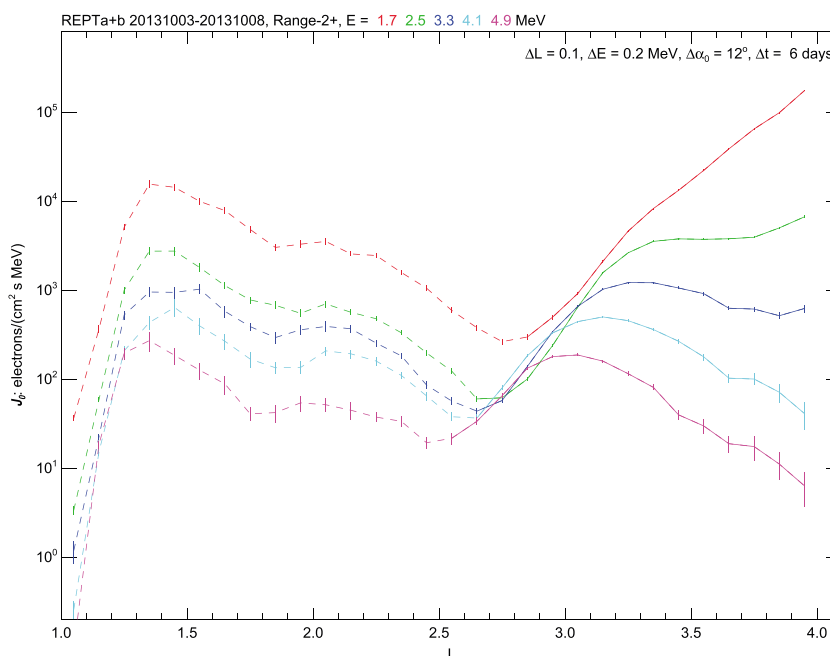


Figure 9. Average omnidirectional equatorial intensity of REPT PHA events identified tentatively as electrons versus L during 3 through 8 October 2013, for selected color-coded electron energies. Dashed lines indicate where the identification is considered unreliable and the data likely result from high-energy protons.

Electron omnidirectional differential intensity from the AE8 and AE9 empirical models are shown as a function of L in Figure 10, at the same selected energies as in Figure 9. The modeled inner zone peak intensity near $L=1.5$ is seen to be significantly higher than the upper limits derived from REPT data, at least for $E \leq 3$ MeV.

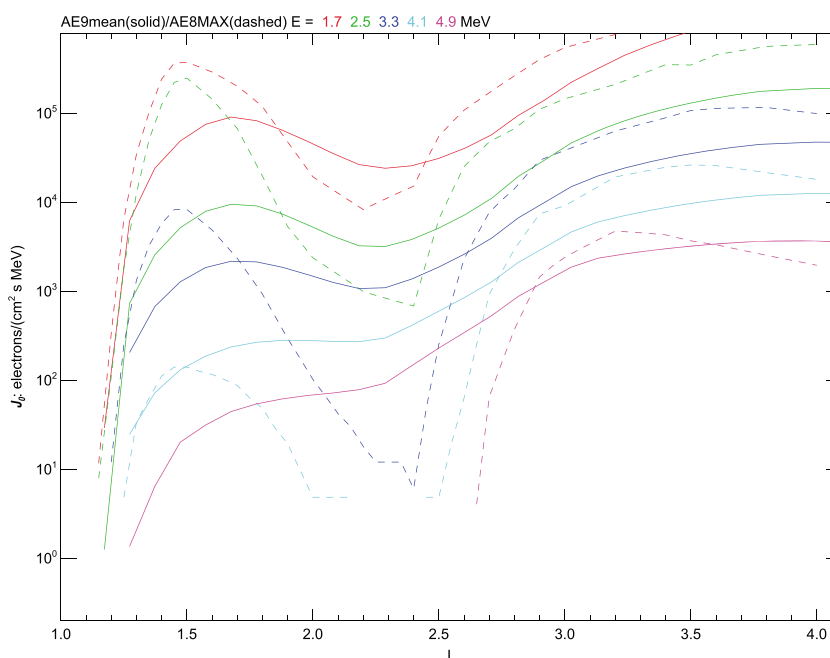


Figure 10. Omnidirectional equatorial electron intensity from the AE8MAX (dashed lines) and AE9 V1.2 (solid lines) radiation belt models, in the same format as Figure 9. The AE8MAX (solar maximum) model differs from the AE8MIN (solar minimum) model only for $L > 2.5$. For the AE9 model, mean values are shown.

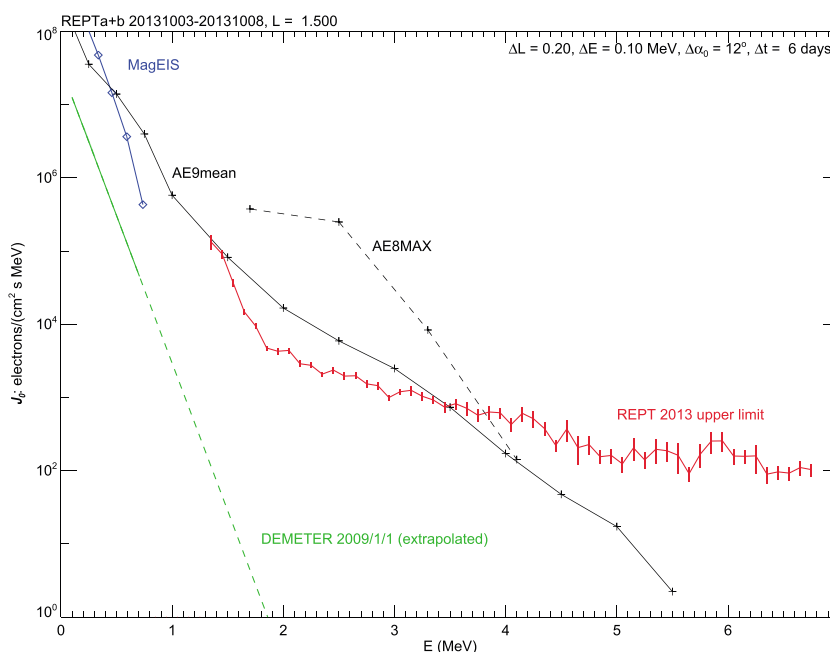


Figure 11. Omnidirectional equatorial electron energy spectra at $L = 1.5$. The average spectrum derived from REPT PHA data (red) likely results from high-energy protons rather than electrons and therefore is an upper limit on the actual electron intensity. Bin widths used in the data analysis are listed. Equivalent model spectra from AE9 V1.2 (solid black) and AE8MAX (dashed black) are shown for comparison. Also shown are MagEIS data (blue) of selected energy channels during the period of 24 February to 1 March 2013 and the exponential energy spectrum measured on the low-altitude (not equatorial) DEMETER satellite during January 2009 for $E < 0.8$ MeV (solid green) and extrapolated to higher energies (dashed green).

The derived upper limit on the omnidirectional differential intensity for $L = 1.5$ is shown as a function of E in Figure 11 (red line). The intensity from the AE8 (dashed black line) and AE9 (black line) models are shown for comparison. Also shown are MagEIS data (blue) of selected energy channels during the period of 24 February to 1 March 2013 and an exponential energy spectrum (green line) derived from data taken on the low-altitude DEMETER satellite during 2009 [Selesnick, 2012]. Those are reliable measurements of electron intensity for $E < 800$ keV, and an extrapolation to higher energies (dashed green line) is well below the upper limits derived from REPT data.

8. Discussion

There are abundant sub-MeV electrons in the inner radiation belt, as demonstrated by CSSWE/REPTile measurements shown in Figures 1 and 2. These are consistent with previous studies using DEMETER measurements: (1) Selesnick [2012] modeled the precipitation loss of hundreds of keV electrons during the quiet year of 2009 and concluded that significant inward radial diffusion must be taking place to replenish the electron population, (2) Zhao and Li [2013a] modeled fast injections of hundreds of keV electrons during a more active year of 2001 and concluded that the fast enhancements of the electrons in the inner belt can be modeled by inward radial diffusion but the diffusion coefficients must be greater and more dynamic than what is commonly thought. However for MeV electrons, it is much more difficult to transport them inward, which is also illustrated and discussed in a recent paper by Baker *et al.* [2014].

Also the high-quality measurements of the Magnetic Electron Ion Spectrometer, MagEIS, instrument [Blake *et al.*, 2013] onboard Van Allen Probes, which was designed so it could correct for proton backgrounds in the inner zone, enabled detailed studies of the PADs of ≤ 600 keV electrons in the inner belt, and Zhao *et al.* [2014a, 2014b] described unusual PADs there that 90 minimum PADs dominate during injection times and normal PADs dominate during quiet times. It is clear that these ≤ 600 keV electrons have fluxes significantly higher than the background noise.

Fennell *et al.* [2015] have shown that the energy spectrum of relativistic electrons in the inner belt is very steep and the flux of ≥ 800 keV electrons are already at the background noise level of the MagEIS, while the flux of < 400 keV electrons is even higher than the AE9 mean value as shown in Figure 11.

However, AE8 and AE9 predict much higher MeV electron fluxes (< 3 MeV) in the inner belt than the upper limit bounded by REPT. We can provide two explanations for the discrepancies: (1) the models are based on data from early years when there had been more deep injections of MeV electrons [Blake *et al.*, 1992; Baker *et al.*, 2004] and there have not been any events as strong as those in terms of interplanetary shock speed and geomagnetic storm intensity in the years just before and during the Van Allen Probes era; and (2) the proton contamination on previous data used for the model building may not have been removed properly.

REPT represents a state-of-art instrument for accurately measuring the energetic particles in the magnetosphere—both REPT instruments on the twin Van Allen Probes show identical features throughout their entire orbits, including the outer belt, slot region, and the inner belt. This, supported by the high-quality measurements of the MagEIS instruments that show no measurable > 800 keV electrons in the inner belt [Fennell *et al.*, 2015], leaves little doubt that the upper limits of MeV electrons bounded by REPT measurements should be the standard for future model improvement, at least for periods like the last few years when no extreme solar wind conditions were observed.

9. Conclusion

Concurrent measurements of relativistic electrons by REPTile and REPT have been analyzed with the focus on the upper limit of MeV electrons in the inner belt. While there are abundant sub-MeV electrons (< 600 keV) in the inner belt, the intensity of > 1 MeV electrons can only be bounded by upper limits (the actual MeV electron flux level is likely much lower), which are significantly lower than intensity levels predicted by AE8 and AE9 models. This finding is significant for two reasons: (1) it shows that unless there are extreme solar wind conditions, such as strong interplanetary shocks and large coronal mass ejections, which have not happened yet since the launch of Van Allen Probes, significant enhancements of MeV electrons do not occur in the inner belt even though such enhancements are commonly seen in the outer belt; and (2) it also suggests that deep dielectric discharging due to MeV electrons is not a concern for satellites in the inner belt region, at least not during the phase of solar cycle where strong interplanetary shocks and large coronal mass ejections are much less likely.

Acknowledgments

We thank Bob Johnston for help with the AE9 V1.2 model. This work was supported in part by NASA agreement NNN14AX181 with the Air Force Research Laboratory under the Heliophysics Guest Investigators Program, at University of Colorado by RBSP-ECT funding through JHU/APL contract 967399 under prime NASA contract NASS-01072, NSF (CubeSat program) grant AGSW 0940277, and a subcontract (FA9453-14-M-0256) from the Air Force Research Laboratory. Van Allen Probes REPT and ephemeris data are available from the ECT Science Operations and Data Center, <http://www.rbsp-ect.lanl.gov>; CSSWE/REPTile and ephemeris data are available from NASA/CDAWeb database, [http://cdaweb.gsfc.nasa.gov/istp/\\$_public/](http://cdaweb.gsfc.nasa.gov/istp/$_public/).

Yuming Wang thanks the reviewers for their assistance in evaluating this paper.

References

- Agostinelli, S., et al. (2003), Nuclear instruments and methods in Physics Research section A: Accelerators, spectrometers, detectors and associated equipment, *Nucl. Instrum. Methods Phys. Res., Sect. A*, 506, 250–303.
- Baker, D. N., S. G. Kanekal, X. Li, S. P. Monk, J. Goldstein, and J. L. Burch (2004), An extreme distortion of the Van Allen belt arising from the 'Halloween' solar storm in 2003, *Nature*, 432, 878–881, doi:10.1038/nature03116.
- Baker, D. N., S. G. Kanekal, R. B. Horne, N. P. Meredith, and S. A. Glauert (2007), Low-altitude measurements of 26 MeV electron trapping lifetimes at $1.5 \leq L \leq 2.5$, *Geophys. Res. Lett.*, 34, L20110, doi:10.1029/2007GL031007.
- Baker, D. N., et al. (2012), The Relativistic Electron-Proton Telescope (REPT) instrument on board the Radiation Belt Storm Probes (RBSP) spacecraft: Characterization of Earth's radiation belt high-energy particle populations, *Space Sci. Rev.*, 179, 337–381, doi:10.1007/s11214-012-9950-9.
- Baker, D. N., et al. (2014), An impenetrable barrier to ultra-relativistic electrons in the Van Allen radiation belt, *Nature*, 515, 531–534, doi:10.1038/nature13956.
- Blake, J. B., W. A. Kolasinski, R. W. Fillius, and E. G. Mullen (1992), Injection of electrons and protons with energies of tens of MeV into $L < 3$ on March 24, 1991, *Geophys. Res. Lett.*, 19, 821–824, doi:10.1029/92GL00624.
- Blake, J. B., et al. (2013), The Magnetic Electron Ion Spectrometer (MagEIS) instruments aboard the radiation belt storm probes (RBSP) spacecraft, *Space Sci. Rev.*, 179(1–4), 383–421, doi:10.1007/s11214-013-9991-8.
- Bichsel, H. (1988), Straggling in thin silicon detectors, *Rev. Mod. Phys.*, 60, 663–699, doi:10.1103/RevModPhys.60.663.
- Funstein, H. O., et al. (2013), Helium, Oxygen, Proton, and Electron (HOPE) mass spectrometer for the radiation belt storm probes mission, *Space Sci. Rev.*, 179, 423–484, doi:10.1007/s11214-013-9968-7.
- Fennell, J. F., S. G. Claudepierre, J. B. Blake, T. P. O'Brien, J. H. Clemmons, D. N. Baker, H. E. Spence, and G. D. Reeves (2015), Van Allen Probes show the inner radiation zone contains no MeV electrons: ECT/MagEIS data, *Geophys. Res. Lett.*, doi:10.1002/2014GL062874.
- Ginet, G. P., et al. (2013), AE9, AP9 and SPM: New models for specifying the trapped energetic particle and space plasma environment, *Space Sci. Rev.*, 179, 579–615, doi:10.1007/s11214-013-9964-y.
- Horne, R. B., et al. (2005), Wave acceleration of electrons in the Van Allen radiation belts, *Nature*, 437, 227–230, doi:10.1038/nature03939.
- Kessel, R. L., N. J. Fox, and M. Weiss (2012), The Radiation Belt Storm Probes (RBSP) and space weather, *Space Sci. Rev.*, 179, 531–543, doi:10.1007/s11214-012-9953-6.
- Kim, K.-C., and Y. Shprits (2012), Radial gradients of phase space density in the inner electron radiation, *J. Geophys. Res.*, 117, A12209, doi:10.1029/2012JA018211.
- Kress, B. T., M. K. Hudson, M. D. Looper, J. Albert, J. G. Lyon, and C. C. Goodrich (2007), Global MHD test particle simulations of > 10 MeV radiation belt electrons during storm sudden commencement, *J. Geophys. Res.*, 112, A09215, doi:10.1029/2006JA012218.
- Li, X., and M. A. Temerin (2001), The electron radiation belt, *Space Sci. Rev.*, 95(1–2), 569–580, (a solicited review paper).

- Li, X., I. Roth, M. Temerin, J. Wygant, M. K. Hudson, and J. B. Blake (1993), Simulation of the prompt energization and transport of radiation particles during the March 24, 1991 SSC, *Geophys. Res. Lett.*, *20*, 2423–2426, doi:10.1029/93GL02701.
- Li, X., A. B. Barker, D. N. Baker, W. C. Tu, T. E. Sarris, R. S. Selesnick, R. Friedel, and C. Shen (2009), Modeling the deep penetration of outer belt electrons during the “Halloween” magnetic storm in 2003, *Space Weather*, *7*, S02004, doi:10.1029/2008SW000418.
- Li, X., S. Palo, R. Kohnert, D. Gerhardt, L. Blum, Q. Schiller, D. Turner, W. Tu, N. Sheiko, and C. S. Cooper (2012), Colorado Student Space Weather Experiment: Differential flux measurements of energetic particles in a highly inclined low Earth orbit, in *Dynamics of the Earth's Radiation Belts and Inner Magnetosphere*, *Geophys. Monogr. Ser.*, vol. 199, edited by D. Summers, pp. 385–404, AGU, Washington, D. C., doi:10.1029/2012GM001313.
- Li, X., S. Palo, R. Kohnert, L. Blum, D. Gerhardt, Q. Schiller, and S. Califf (2013a), Small mission accomplished by students—Impact on space weather research, *Space Weather*, *11*, 55–56, doi:10.1002/swe.20025.
- Li, X., et al. (2013b), First results from CSSWE CubeSat: Characteristics of relativistic electrons in the near-Earth environment during the October 2012 magnetic storms, *J. Geophys. Res. Space Physics*, *118*, 6489–6499, doi:10.1002/2013JA019342.
- Lenchek, A. M., S. F. Singer, and R. C. Wentworth (1961), Geomagnetically trapped electrons from cosmic ray albedo neutrons, *J. Geophys. Res.*, *66*(12), 4027–4046, doi:10.1029/JZ066i012p04027.
- Lyons, L. R., and R. M. Thorne (1973), Equilibrium structure of radiation belt electrons, *J. Geophys. Res.*, *78*, 2142–2149, doi:10.1029/JA078i013p02142.
- Looper, M. D., J. B. Blake, R. A. Mewaldt, J. R. Cummings, and D. N. Baker (1994), Observations of the remnants of the ultrarelativistic electrons injected by the strong SSC of 24 March 1991, *Geophys. Res. Lett.*, *21*, 2079–2082, doi:10.1029/94GL01586.
- Mauk, B. H., N. J. Fox, S. G. Kanekal, R. L. Kessel, D. G. Sibeck, and A. Ukhorskiy (2012), Science objectives and rationale for the radiation belt storm probes mission, *Space Sci. Rev.*, *179*, 3–27, doi:10.1007/s11214-012-9908-y.
- Rosen, A., and N. L. Sanders (1971), Loss and replenishment of electrons in the inner radiation zone during 1965–1967, *J. Geophys. Res.*, *76*(1), 110–121, doi:10.1029/JA076i001p00110.
- Vette, J. I. (1991), The AE-8 trapped electron model environment, *NSSDC/WDC-A-R&S 91–24*, NASA Goddard Space Flight Center, Greenbelt, Md.
- Schiller, Q., and A. Mahendrakumar (2010), REPTile: A miniaturized detector for a CubeSat mission to measure relativistic particles in near-Earth space, paper SSC10-VIII-1 presented at 24th Annual AIAA/USU Conference on Small Satellites, Frank J. Redd Student Scholarship Competition, Logan, Utah, USA, Aug. 9–12, 2010.
- Schorr, B. (1974), Programs for the Landau and the Vavilov distributions and the corresponding random numbers, *Comput. Phys. Commun.*, *7*, 215–224.
- Selesnick, R. S. (2006), Source and loss rates of radiation belt relativistic electrons during magnetic storms, *J. Geophys. Res.*, *111*, A04210, doi:10.1029/2005JA011473.
- Selesnick, R. S. (2012), Atmospheric scattering and decay of inner radiation belt electrons, *J. Geophys. Res.*, *117*, A08218, doi:10.1029/2012JA017793.
- Selesnick, R. S., D. N. Baker, A. N. Jaynes, X. Li, S. G. Kanekal, M. K. Hudson, and B. T. Kress (2014), Observations of the inner radiation belt: CRAND and trapped solar protons, *J. Geophys. Res. Space Physics*, *119*, 6541–6552, doi:10.1002/2014JA020188.
- Selesnick, R. S., M. D. Looper, and R. A. Mewaldt (2007), A theoretical model of the inner proton radiation belt, *Space Weather*, *5*, S04003, doi:10.1029/2006SW000275.
- Spence, H. E., et al. (2013), Science goals and overview of the Radiation Belt Storm Probes (RBSP) Energetic Particle, Composition, and Thermal Plasma (ECT) suite on Nasa's Van Allen Probes mission, *Space Sci. Rev.*, *179*, 311–336, doi:10.1007/s11214-013-0007-5.
- Tu, W., R. Selesnick, X. Li, and M. Looper (2010), Quantification of the precipitation loss of radiation belt electrons observed by SAMPEX, *J. Geophys. Res.*, *115*, A07210, doi:10.1029/2009JA014949.
- Zhao, H., and X. Li (2013a), Inward shift of outer radiation belt electrons as a function of *Dst* index and the influence of the solar wind on electron injections into the slot region, *J. Geophys. Res. Space Physics*, *118*, 756–764, doi:10.1029/2012JA018179.
- Zhao, H., and X. Li (2013b), Modeling energetic electron penetration into the slot region and inner radiation belt, *J. Geophys. Res. Space Physics*, *118*, 6936–6945, doi:10.1002/2013JA019240.
- Zhao, H., X. Li, J. B. Blake, J. F. Fennell, S. G. Claudepierre, D. N. Baker, A. N. Jaynes, D. M. Malaspina, and S. G. Kanekal (2014a), Peculiar pitch angle distribution of relativistic electrons in the inner radiation belt and slot region, *Geophys. Res. Lett.*, *41*, 2250–2257, doi:10.1002/2014GL059725.
- Zhao, H., X. Li, J. B. Blake, J. F. Fennell, S. G. Claudepierre, D. N. Baker, A. N. Jaynes, and D. M. Malaspina (2014b), Characteristics of pitch angle distributions of 100s keV electrons in the slot region and inner radiation belt, *J. Geophys. Res. Space Physics*, *119*, 9543–9557, doi:10.1002/2014JA020386.

RESEARCH ARTICLE

10.1002/2014JA020188

Special Section:

New Perspectives on Earth's Radiation Belt From the Prime Mission of the Van Allen Probes

Key Points:

- Radiation belt protons have been measured by Van Allen Probes/REPT
- High-energy proton contamination is removed by a probabilistic analysis method
- Pitch angle distributions reveal CRAND and solar origins of trapped protons

Correspondence to:

R. S. Selesnick,
richard.selesnick@us.af.mil

Citation:

Selesnick, R. S., D. N. Baker, A. N. Jaynes, X. Li, S. G. Kanekal, M. K. Hudson, and B. T. Kress (2014), Observations of the inner radiation belt: CRAND and trapped solar protons, *J. Geophys. Res. Space Physics*, 119, doi:10.1002/2014JA020188.

Received 16 MAY 2014

Accepted 1 AUG 2014

Accepted article online 6 AUG 2014

Observations of the inner radiation belt: CRAND and trapped solar protons

R. S. Selesnick¹, D. N. Baker², A. N. Jaynes², X. Li^{2,3}, S. G. Kanekal⁴, M. K. Hudson⁵, and B. T. Kress⁵
¹Space Vehicles Directorate, Air Force Research Laboratory, Kirtland AFB, New Mexico, USA, ²Laboratory for Atmospheric and Space Physics, University of Colorado Boulder, Boulder, Colorado, USA, ³Department of Aerospace Engineering Sciences, University of Colorado Boulder, Boulder, Colorado, USA, ⁴NASA/Goddard Space Flight Center, Greenbelt, Maryland, USA, ⁵Department of Physics and Astronomy, Dartmouth College, Hanover, New Hampshire, USA

Abstract Measurements of inner radiation belt protons have been made by the Van Allen Probes Relativistic Electron-Proton Telescopes as a function of kinetic energy (24 to 76 MeV), equatorial pitch angle, and magnetic L shell, during late 2013 and early 2014. A probabilistic data analysis method reduces background from contamination by higher-energy protons. Resulting proton intensities are compared to predictions of a theoretical radiation belt model. Then trapped protons originating both from cosmic ray albedo neutron decay (CRAND) and from trapping of solar protons are evident in the measured distributions. An observed double-peaked distribution in L is attributed, based on the model comparison, to a gap in the occurrence of solar proton events during the 2007 to 2011 solar minimum. Equatorial pitch angle distributions show that trapped solar protons are confined near the magnetic equator but that CRAND protons can reach low altitudes. Narrow pitch angle distributions near the outer edge of the inner belt are characteristic of proton trapping limits.

1. Introduction

The inner radiation belt includes an intense population of high-energy protons (~ 10 MeV to 1 GeV) trapped by the geomagnetic field below altitudes $\sim 10^4$ km. The hazard these protons present to spacecraft has precluded their detailed study, although many coarse measurements were made early in the space age (summarized by Sawyer and Vette [1976]). In more recent times, only the CRRES satellite has made inner-belt proton measurements near the geomagnetic equatorial plane, where the entire trapped population is accessible [Gussenhoven *et al.*, 1996]. Low-altitude satellites provide only a limited view [Looper *et al.*, 1998]. However, there is still considerable interest in developing an accurate model of the trapped proton distribution to aid in spacecraft design [Ginet *et al.*, 2013].

The sources of inner-belt protons are cosmic ray albedo neutron decay (CRAND) and interplanetary solar protons. The CRAND mechanism is well understood, but that of solar proton trapping is not. Other significant processes, such as radial diffusion and losses during magnetic storms, are recognized only empirically. Theoretical modeling of the inner belt therefore includes several free parameters that are adjusted to match the limited available data [Vacaresse *et al.*, 1999; Selesnick *et al.*, 2007, 2013]. Detailed new measurements of the trapped proton distribution would be of value in constraining both the empirical and theoretical models and in testing theories of inner-belt source, loss, and transport processes.

New measurements of the inner radiation belt are now being made by NASA's Van Allen Probes (formerly known as Radiation Belt Storm Probes or RBSP), launched in August 2012 [Mauk *et al.*, 2012]. The two satellites are in similar elliptical, near-equatorial orbits and carry instrumentation of identical design. Proton data with high resolution in kinetic energy (~ 24 to 76 MeV), pitch angle, and magnetic L shell are available from the Relativistic Electron-Proton Telescope (REPT) [Baker *et al.*, 2012].

The subject of this work is interpretation of the pulse-height analyzed (PHA) data from REPT, available at a rate sufficient for detailed studies since October 2013. The data analysis method is described in section 2, with emphasis on the elimination of background caused by high-energy particles that is a particular problem for inner-belt measurements. Results of the data analysis, which show the proton distribution as a function of L shell, kinetic energy, and equatorial pitch angle, from 3 October 2013 through 21 March 2014, are described in section 3. The proton distribution predicted by a theoretical inner-belt model is described in

section 4. Finally, section 5 discusses implications of the results based on comparison of the measurements to the model predictions.

2. Data Analysis

The analysis method adopted for the REPT PHA data is based on a probabilistic approach that has been described in detail by *Selesnick* [2014]. Application of the method to REPT data is summarized below, beginning with a brief description of the telescope design.

Each REPT contains a series of nine aligned planar Si detectors, called R1 to R9. The front two have 1.5 mm thickness and 20 mm diameter; the following seven have 3 mm thickness and 40 mm diameter. (The thicker detectors, R3 to R9, combine two 1.5 mm Si wafers. The front detector, R1, is divided into two active areas, but in this work their data are combined as if it were a single detector.) A collimated aperture allows a 32° field of view (FOV). A 2 mm thick Be window inside the collimator shields the front detector from low-energy particles, while Al and W shielding stops electrons and lower energy protons ($\lesssim 100$ MeV) from outside the FOV.

The REPT detectors are closely spaced, in a configuration ideal for electron measurements because it limits the effect of scattering. This configuration does not exclude high-energy protons from outside the FOV. The inner radiation belt contains many such high-energy protons ($\gtrsim 100$ MeV) that, after losing energy in the Al and W shielding, can mimic the signal of lower energy protons. It is necessary to exclude them from the data.

The PHA data from a single charged particle consist of a set of data numbers (DN) that are proportional to the energy deposit, or energy lost by the particle, in each detector. (The conversion from DN to energy loss Δ in MeV is $\Delta \approx \text{DN}/38$, but, because each detector has its own analysis chain, there is an accurate conversion for each detector. It is calibrated from data showing the DN for end-of-range protons and the known proton energy required to have a range equal to the detector thickness.)

A proton entering the front detector can also trigger some number of the subsequent detectors, depending on the proton's original kinetic energy E and incidence angle θ , before either stopping in the final detector triggered or exiting through the side of the telescope. If it triggers detectors R1 through R n then the set of measured energy losses $\{\Delta_1 \dots \Delta_n\}$ is called an event of Range- n .

Protons lose energy in Si at a rate described by the range-energy relationship, $R_{\text{Si}}(E)$, but the rate also fluctuates in a process called range straggling. The probability density function (PDF) for energy loss Δ in a path length x from an incident energy E is called the straggling function, $f(\Delta, E, x)$ [Bichsel, 1988].

For detector i the path length is $x = x_i \sec \theta$, where x_i is the detector thickness. The energy is reduced from its value E_0 prior to entering the first detector by losses in intervening detectors. The energy losses are independent random processes; therefore, for a given event, or set of measured Δ_i , and assuming no prior knowledge of E_0 and θ , the PDF for E_0 and θ is the product of straggling functions from each detector:

$$f_n(E_0, \theta) = \prod_{i=1}^n f(\Delta_i, E_0 - E_{i-1}, x_i \sec \theta) \quad (1)$$

where the total energy loss up to detector i is

$$E_i = \sum_{j=1}^i \Delta_j \quad (2)$$

If the proton of a given event stopped in detector k , then straggling in that detector is irrelevant, because the proton lost its remaining energy there, and $n = k - 1$. The proton's incident energy at the first detector is the total energy loss $E_0 = E_k$.

The proton's energy E prior to entering REPT was higher by the amount lost in the Be window. Since this amount is unknown, the energy in space is estimated as $E = R_{\text{Be}}^{-1}(R_{\text{Be}}(E_k) + x_w)$, where $R_{\text{Be}}(E_k)$ is the proton range in Be for initial energy E_k , R_{Be}^{-1} is its inverse, and x_w is the thickness of the Be window. Because the energy loss in the window is a small fraction of E_k , the uncertainty in this estimate is small.

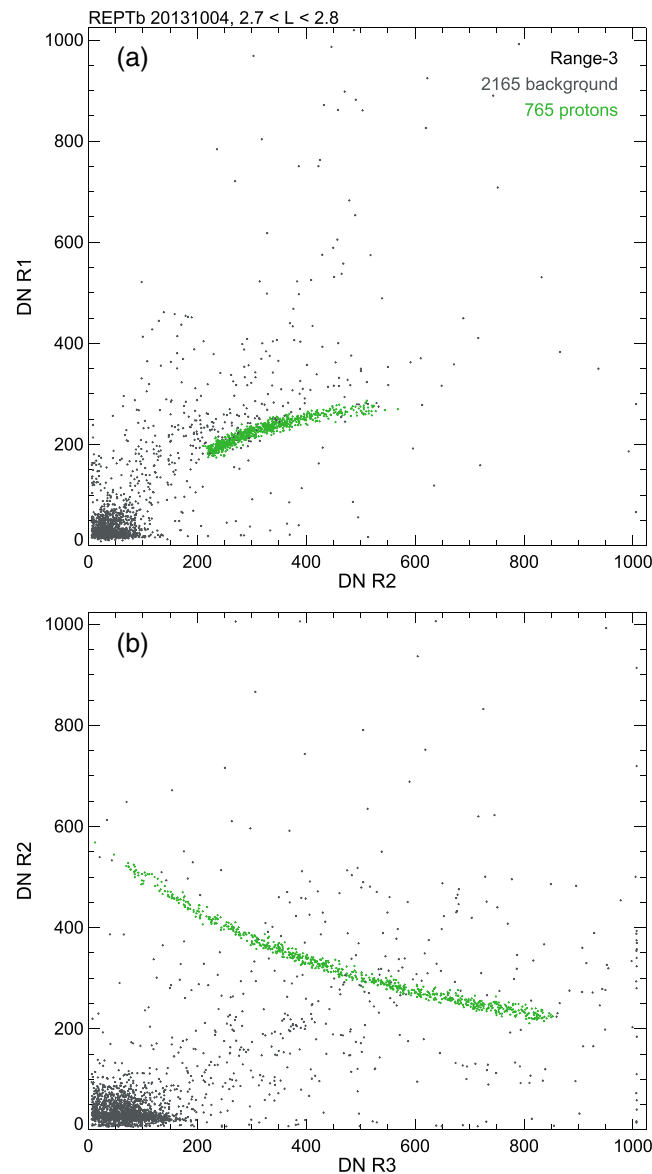


Figure 1. Range-3 PHA event data from REPT-B obtained in the outer part of the inner radiation belt on 4 October 2013. (a) Data numbers (DN) from detector R1 versus those from detector R2 and (b) similarly for detectors R2 and R3. The DN values are proportional to energy deposit in each detector. The total number of identified valid proton events (green) and background or all other events (gray) are listed.

In applying the data reduction procedure just described, proton ranges in Si and Be were obtained from the NIST/PSTAR (National Institute of Standards and Technology, Stopping-Power and Range Tables for Protons) tabulation [Berger *et al.*, 2011]. For the straggling function f , approximations were adopted based on the value of the Vavilov parameter κ [Chibani, 1998]. (For $\kappa > 10$, which occurs near the end of the proton range, f approximates a Gaussian distribution. However, the approximations are invalid when the energy loss Δ is close to the incident energy E , and the Gaussian distribution then appears too narrow for low energy losses in the stopping detector. An empirical correction was found by adding $0.3(\kappa/10 - 1)$ MeV in quadrature with the standard deviation of the Gaussian. This broadened the distribution sufficiently but increased the number of retained events by only $\sim 1\%$, illustrating the robustness of the method.)

The reduced data set contains only valid proton PHA events, those PHA events estimated to have resulted from protons that were in the FOV and stopped in one of detectors R2 through R9. The kinetic energy range of such protons is ~ 24 to 76 MeV.

The incident angle θ is unknown, but, assuming it is in the FOV (that is, the proton entered through the collimator), the angle can be estimated as the mean of the distribution:

$$\bar{\theta} = \frac{\int_0^{\theta_m} \theta f_{k-1}(E_k, \theta) d\theta}{\int_0^{\theta_m} f_{k-1}(E_k, \theta) d\theta} \quad (3)$$

where $\theta_m = 16^\circ$ is the collimator half-angle.

Protons from outside the FOV have $\theta > \theta_m$ and may or may not have stopped in detector k . Such events should be discarded. First, the residual range of the proton at detector k should be less than the required path length, $R_{Si}(\Delta_k) < x_k \sec \bar{\theta}$. If it is not, then there is a high likelihood that the proton did not stop and the event is discarded. Second, the probability density evaluated with the estimated parameters should be greater than a minimum value, $f_{k-1}(E_k, \bar{\theta}) > f_{\min}$. If it is not, then there is a high likelihood that the proton had $\theta > \theta_m$, and the event is discarded. The value for the minimum probability, found by trial and error as described below, is $f_{\min} = 10^{-3}$. Low- and high-probability events generally are well separated by this procedure, and results are insensitive to the exact value of f_{\min} .

Protons with high enough energy to penetrate all nine detectors without stopping are eliminated from the data by the above procedure, whether or not they were in the FOV. For such events in the FOV it is possible to accurately estimate their energy [Selesnick, 2014]. However, it is difficult to distinguish them from protons outside the FOV and this is not attempted here.

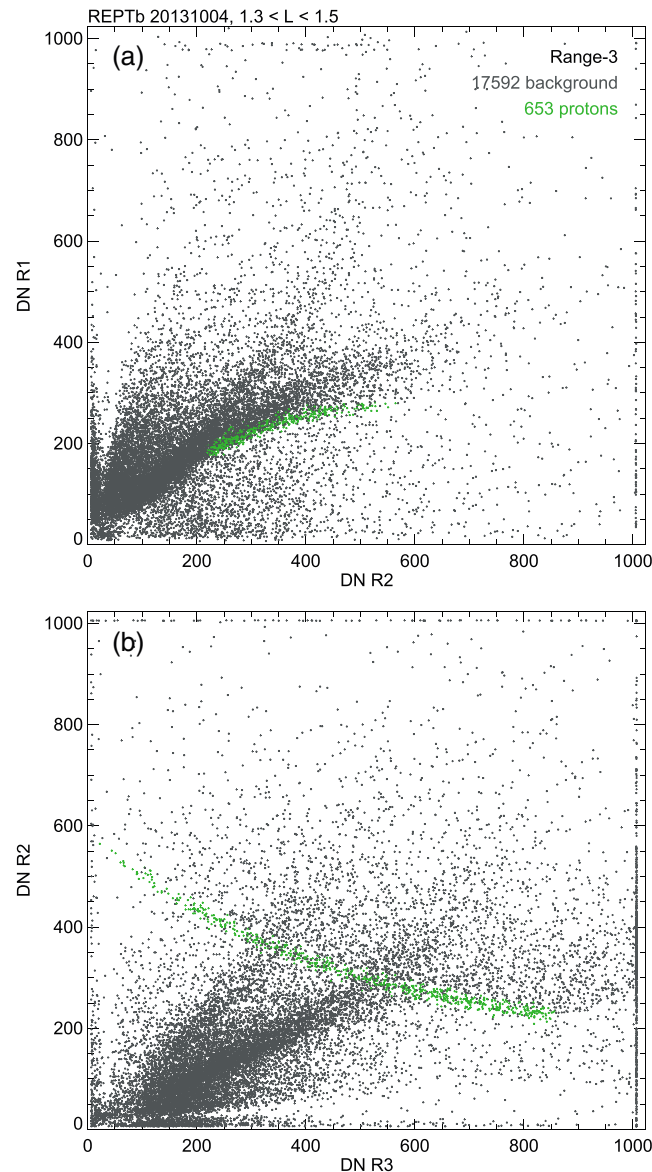


Figure 2. Similar to Figure 1, but data were obtained near the middle of the inner radiation belt.

These create a dense background, but there is no difficulty in finding the valid proton events (green in the figure) even though they are a small fraction of the total. Background events above and to the right of the valid proton track in R2 versus R3 (Figure 2b) result primarily from protons that stopped in R3 but were outside the FOV. Those below and to the left result primarily from protons that did not stop in R3 but had a high enough incidence angle to avoid R4, and they may have entered from the front or the back. There are also some background events created by protons crossing an edge of one or more detectors, resulting in low energy deposits.

After valid proton events have been identified, the remainder of the data analysis procedure is relatively straightforward. Using the reduced data set, the equatorial differential unidirectional proton intensity (or flux) j_0 is related to the number of valid proton events N in a given interval Δt of time t , ΔE of energy E , $\Delta \alpha_0$ of equatorial pitch angle α_0 , and ΔL of L shell:

$$j_0(t, E, \alpha_0, L) = \frac{\delta t}{e G \Delta t \Delta E} \sum_{i=1}^N r_i \quad (4)$$

The effectiveness of the data reduction method for selecting valid proton events is illustrated in Figures 1 and 2. Measured DN values are shown from Range-3 events, those with signals in the first three detectors R1, R2, and R3. For each event, the DN value from R1 is shown versus that from R2 (Figures 1a and 2a), as is the DN value from R2 versus that from R3 (Figures 1b and 2b). Valid proton events (green) are distinguished from all other PHA events, labeled as background (gray). The figures show data from REPT-B during 1 day but restricted to different L ranges.

In the outer part of the inner belt (Figure 1, $2.7 < L < 2.8$) there are few high-energy protons, and the valid proton events form a distinct track that has been identified by the data reduction procedure. (Even clearer tracks are evident in solar proton data at high L .) Because events forming the track must have been from protons in the FOV, and the protons must have stopped in R3, such data are useful for calibrating the DN to energy conversion, for verifying the value of f_{\min} , and for empirical correction of straggling functions. The density of background events is low relative to that of valid proton events except where $DN < 200$ in all detectors, a region well separated from the proton track (these events with low energy deposits result from electrons and cosmic ray protons).

Near the center of the inner belt (Figure 2, $1.3 < L < 1.5$) there are many high-energy protons with $E > 100$ MeV.

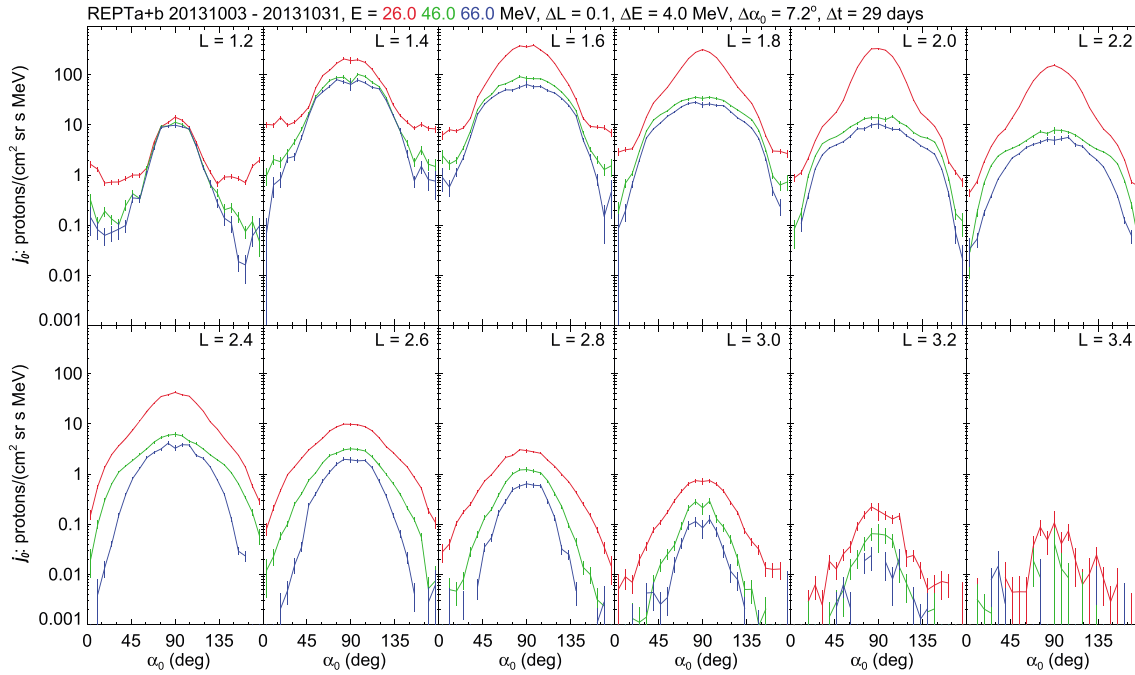


Figure 3. Measured average proton equatorial pitch angle distributions (j_0 versus α_0) during October 2013, at selected L values from 1.2 to 3.4, from a combination of REPT-A and REPT-B data. Three proton energies, identified by color, and bin widths are listed above. Statistical error bars are shown at the center of each α_0 bin.

where $G = 0.2 \text{ cm}^2 \text{ sr}$ is the REPT geometry factor (independent of proton range) and $\epsilon = 1$ is the proton detection efficiency in the FOV. The intervals need not be contiguous. For example, Δt could include all times in a day during which RBSP was within ΔL and REPT was observing protons within $\Delta \alpha_0$. The summation is over observed valid proton events. Pulse-height analysis is initiated within REPT by any count recorded in the first detector R1, but it can happen only once within each time step $\delta t = 12 \text{ ms}$.

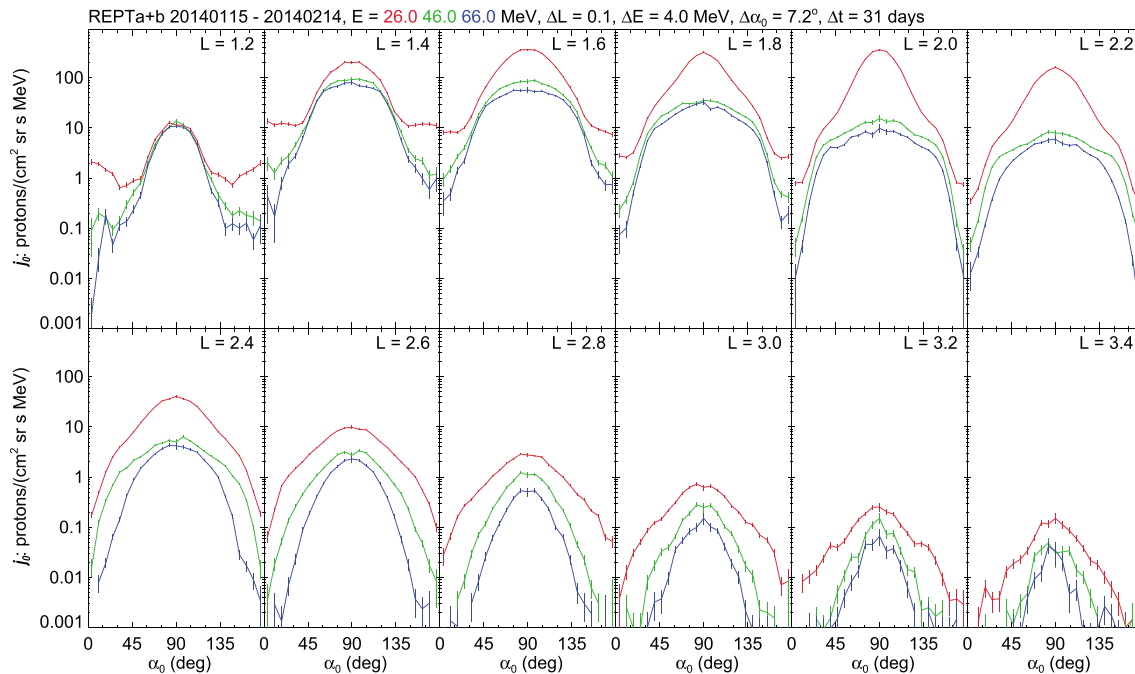


Figure 4. Similar to Figure 3 but for the time interval 15 January to 14 February 2014.

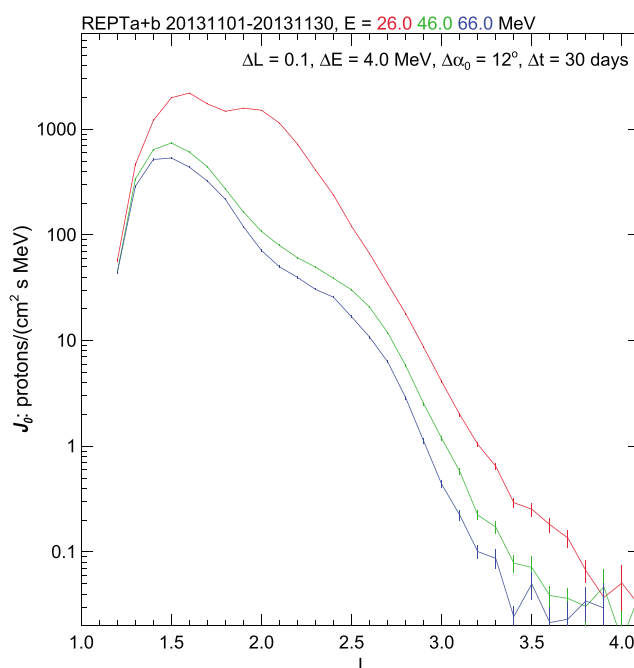


Figure 5. Measured average equatorial differential omnidirectional proton intensity versus L during November 2013, from a combination of REPT-A and REPT-B data. Three proton energies, identified by color, and bin widths are listed above. Statistical error bars are shown at the center of each L bin.

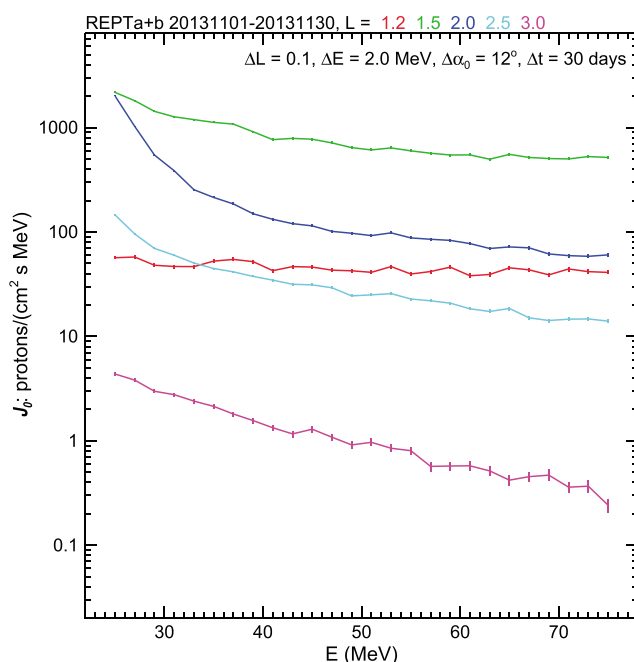


Figure 6. Measured average equatorial omnidirectional proton energy spectra at selected L values during November 2013, from a combination of REPT-A and REPT-B data. Five L values, identified by color, and bin widths are listed above. Statistical error bars are shown at the center of each kinetic energy (E) bin.

The counting rate of R1 at the time of proton event i is r_i and is measured by a counter on REPT. Including it in the summation accounts, on average, for those protons that were not recorded as PHA events during each δt .

During times when R1 is counting fast enough that an event is recorded in every δt , the time of each event is known to an accuracy of 12 ms. (Data from REPT-A in the L range from 2.4 to 3.6 are excluded due to insufficient R1 counting rates. The R1 rates from REPT-B in this L range are higher due to an instrumental effect rather than any difference in the environments of the two spacecraft.) The satellite rotation period is ~ 11 s, so the pointing direction of REPT for a given proton event can be determined with accuracy better than 1° . The local pitch angle of the REPT axis is determined from its direction relative to the magnetic field measured by the Electric and Magnetic Field Instrument Suite and Integrated Science (EMFISIS) magnetometer [Kletzing *et al.*, 2013].

Local pitch angles are converted to equatorial pitch angles α_0 using local and equatorial magnetic field magnitudes from the IGRF+OP77Q (International Geomagnetic Reference Field + Olson-Pfitzer 1977 Quiet) field model [Olson and Pfitzer, 1977]. Values of L are obtained from the same field model for locally mirroring particles and with Earth's dipole moment of 2014. (With this model the McIlwain L_m and the invariant L^* [Roederer, 1970] are nearly identical for $L \lesssim 2$ and differ by < 0.1 for $L \lesssim 3.5$; $L = L_m$ is used.) The L values are evaluated at the satellite locations rather than at the proton gyrocenters, and so intensities are effectively averaged over east-west anisotropies caused by radial gradients.

3. Results

Proton intensities from equation (4) are shown in Figures 3 to 7. All proton events in a given data bin were combined to form an average intensity for

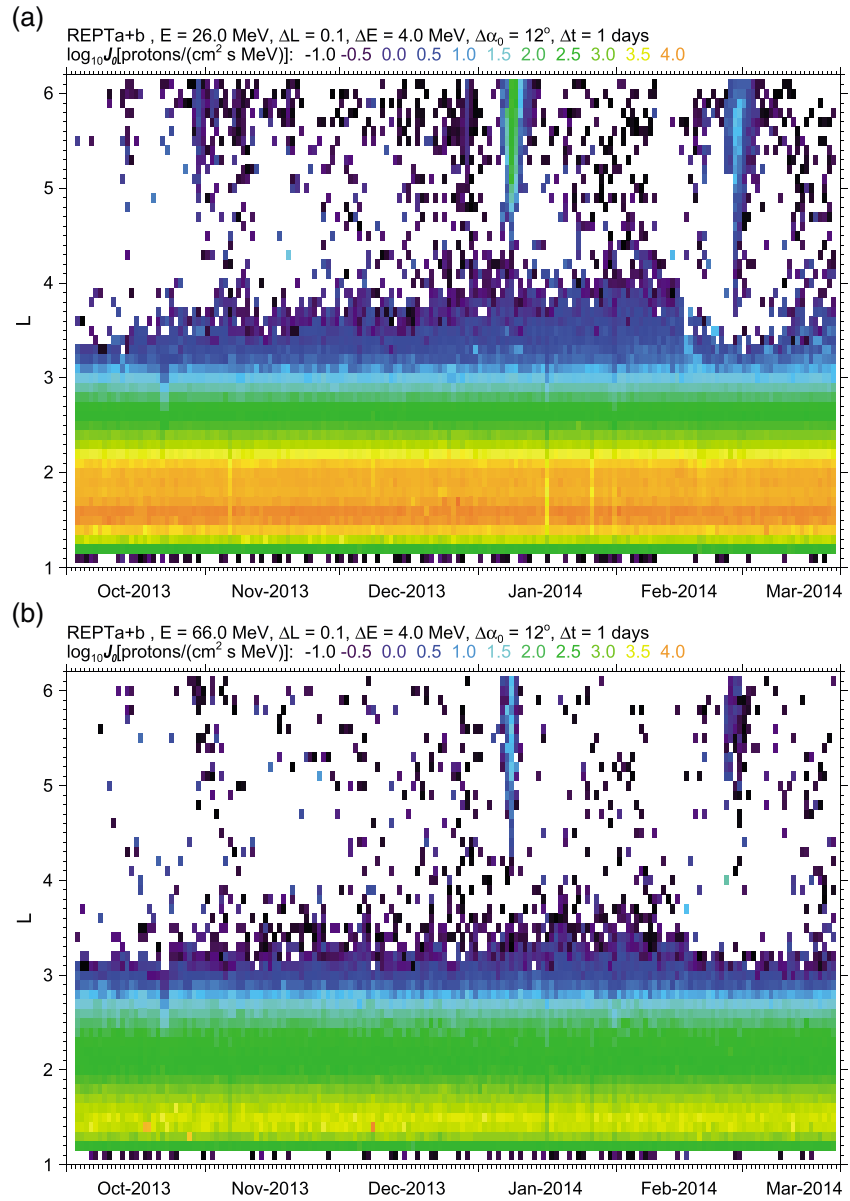


Figure 7. Measured daily average equatorial differential omnidirectional intensity versus L and time from 3 October 2013 to 21 March 2014, for (a) 26 MeV and (b) 66 MeV protons, from a combination of REPT-A and REPT-B data. Intensity color coding and bin widths are listed above.

that bin. This includes data from both spacecraft where available. Statistical 1σ error bars, shown in some of the figures, are j_0 / \sqrt{N} . All L , E , and α_0 values refer to the bin centers; bin widths ΔL , ΔE , $\Delta\alpha_0$, and Δt are indicated in each figure.

In Figures 3 and 4, j_0 is shown as a function of α_0 for selected E and L values, illustrating the varying equatorial pitch angle distributions. Monthly averages ($\Delta t \approx 1$ month), from October 2013 (Figure 3) and January–February 2014 (Figure 4), allow high statistical accuracy in most of the bins. Equatorial pitch angle bins have width $\Delta\alpha_0 = 7.2^\circ$, but bins are assigned according the direction of the REPT axis as described above. Distributions are therefore smoothed as a result of the FOV, reducing pitch angle resolution by $\sim 16^\circ$.

For Figures 5 to 7, j_0 was converted to equatorial differential omnidirectional intensity,

$$J_0 = 2\pi \int_0^\pi j_0 \sin \alpha_0 d\alpha_0 \quad (5)$$

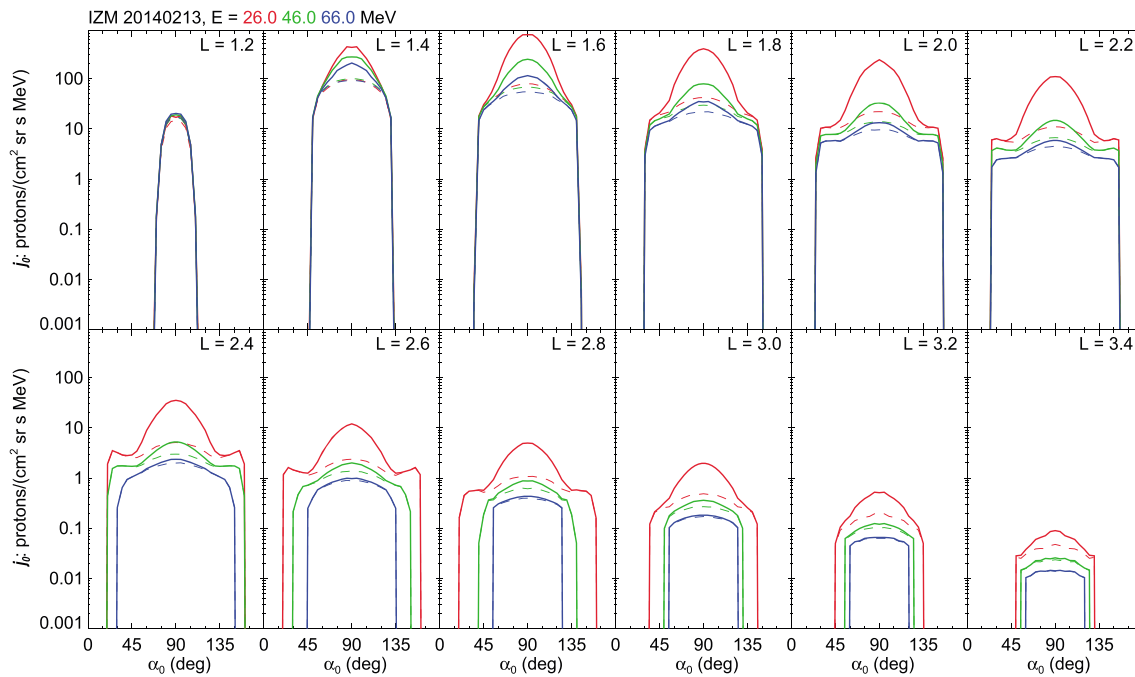


Figure 8. Model proton equatorial pitch angle distributions for 13 February 2014. Three proton energies are identified by color, as in Figures 3 and 4. Solid lines include CRAND and solar proton sources, dashed lines include only the CRAND source. For model description, see *Selesnick et al.* [2007, 2013].

The integral was approximated as a summation over α_0 bins of width $\Delta\alpha_0 = 12^\circ$, and statistical errors for J_0 combine those for each α_0 bin in quadrature.

In Figure 5, J_0 is shown as a function of L for selected E bins. A single time bin for the month of November 2013 again allows high resolution in L and E with high statistical accuracy. In Figure 6, J_0 is shown as a function of E for selected L bins from the same time interval, with higher E resolution to illustrate the changing energy spectra with L .

In Figure 7, J_0 is shown as a function of L and time for 1 day time bins and two selected E bins from 3 October 2013 through 21 March 2014. The higher time resolution in this case means that the statistical accuracy is lower. (Also, varying magnetic coordinates of each satellite means that there are occasional days with incomplete coverage in α_0 , causing sudden artificial changes in J_0 . Similar abrupt changes are also caused by occasional data gaps. Such artificial changes are discernible by their short duration of 1 or 2 days. For Figure 7 only, a few data gaps from REPT-B in the range $2.4 < L < 3.6$ are filled by data from the previous day.) As shown in Figure 7, and by comparison of Figures 3 and 4, there was little or no significant change in proton intensity for $L \lesssim 3$ during the ~ 6 -month period but considerable change for $L \gtrsim 3$. Untrapped solar protons are evident for $L \gtrsim 4$, particularly during the solar proton event of 6 to 10 January 2014.

4. Model Predictions

Because of charged particle effects on spacecraft, significant effort has been expended in developing accurate radiation belt models, both empirical [*Ginet et al.*, 2013] and theoretical [*Vacaresse et al.*, 1999]. For comparison to the REPT inner-belt proton observations, predictions by a recent theoretical model [*Selesnick et al.*, 2007, 2013] are now described. They allow the observations to be interpreted on the basis of current theory.

The model includes the two source processes: CRAND and solar proton trapping. Included loss processes are ionization of the local plasma and neutral atmosphere (Coulomb drag) and inelastic nuclear scattering. Stable trapping limits form the energy and pitch angle dependent model outer boundary. These limits are lowered during magnetic storms, using an empirical dependence on the minimum Dst , causing storm time losses. Radial diffusion is included with coefficient $D_{LL} = 2 \times 10^{-13} L^{10} s^{-1}$ (modified slightly from earlier applications by dropping uncertain energy and pitch angle dependencies). Geomagnetic secular variation

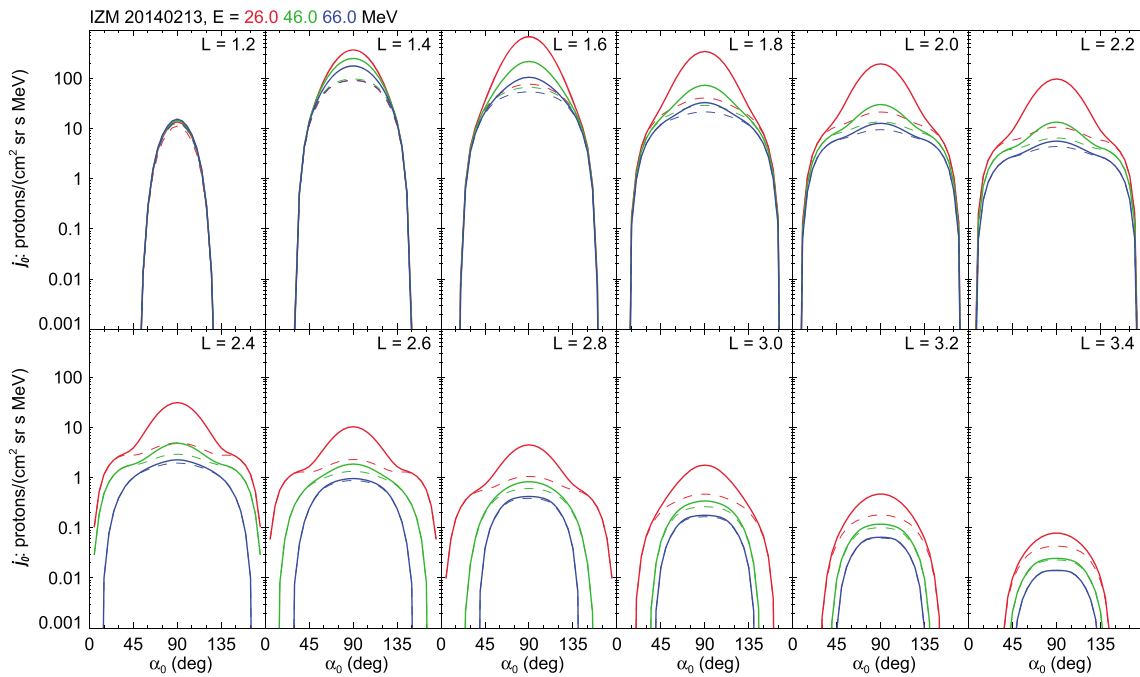


Figure 9. The same model equatorial pitch angle distributions as in Figure 8 but averaged over the REPT field of view (FOV) and over the $7.2^\circ \alpha_0$ bins used in Figures 3 and 4.

is included using historical internal magnetic field models, required because of long proton residence times at some locations.

Trapping of CRAND protons occurs in the model at a nearly steady rate and at all inner-belt locations.

Trapping of solar protons occurs in the model only for $L > 2$ and only at times of historical solar proton events.

After trapping, protons can diffuse radially. Outward diffusion is relatively fast because of the strong L dependence in D_{LL} , but the intensity of trapped solar protons for $L < 2$ is an accumulation over many years due to slow inward diffusion. These protons originate predominantly in the occasional large solar proton events.

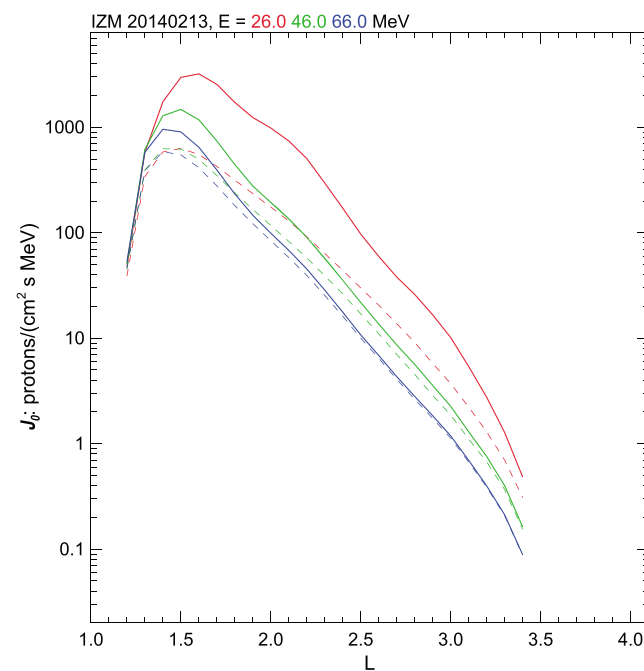


Figure 10. Model proton equatorial omnidirectional intensity versus L , for 13 February 2014. Three proton energies are identified by color, as in Figure 5. Solid lines include solar and CRAND sources; dashed lines include only the CRAND source.

Model equatorial pitch angle distributions are shown in Figure 8. The same distributions, but averaged over the REPT FOV and over bins of width $\Delta \alpha_0 = 7.2^\circ$ (as used in the data analysis), are shown in Figure 9 for comparison to the observations in Figure 4. Also included in Figures 8 and 9 are separate curves (dashed lines) showing the model contribution from the CRAND source alone, excluding trapped solar protons.

Model omnidirectional proton intensity as a function of L at select energies is shown in Figure 10, for comparison to the observations in Figure 5. The contributions of CRAND alone are again indicated.

5. Discussion and Conclusion

The probabilistic data analysis method has proved effective for identifying valid proton events from the REPT PHA data, valid events being from protons that entered the collimator in the FOV, went through the first detector, and stopped in one of the eight subsequent detectors, the intended operating mode for REPT. This was demonstrated using data from the outer part of the inner radiation belt, where there is little contamination from higher-energy protons (Figure 1), and then applied to data from throughout the inner belt, for which there can be substantial contamination (Figure 2).

The method's effectiveness at removing background events caused by high-energy proton contamination is seen in measured equatorial pitch angle distributions (Figures 3 and 4). At low L , some background is still evident in the nonzero measured proton intensity near $\alpha_0 = 0$ and 180° . These low and high pitch angles are well inside the atmospheric loss cones where the trapped proton intensity is expected to be 0, as shown by model calculations (Figure 8). The background is caused by trapped protons entering through the side of REPT, and the pitch angles determined for those protons are therefore inaccurate; hence, they appear in the loss cones. The loss cones are widest and the background is most apparent at the lowest L . Nevertheless, the remaining background there is lower than the measured intensity near $\alpha_0 = 90^\circ$ by factors of ~ 10 to 100, depending on energy. Higher background is seen at lower energy because those measurements depend on a combination of energy loss measurements from fewer detectors. As a fraction of measured trapped proton intensity, background decreases with increasing L .

Elimination of most of the high-energy proton background allowed accurate calculation of omnidirectional intensities, J_0 . Averaging over intervals long enough to minimize statistical errors, and to provide sufficient coverage of the full α_0 range, resulted in accurate equatorial radial profiles of inner-belt protons at fixed energy (Figure 5) and equatorial energy spectra at fixed L (Figure 6).

In the radial profiles, a double-peaked structure is evident at the lower energy (Figure 5, 26 MeV), with a main peak near $L = 1.6$ and a secondary peak near $L = 2$. For the higher energies (46 and 66 MeV) the main peak is near $L = 1.5$ and a secondary bump in the profile appears near $L = 2.5$. These observations are readily interpreted with reference to the model simulations (Figure 10). Although data and model do not agree perfectly, similar structures are evident in each.

The low-energy main peak was formed by inward diffusion of injected solar protons over many years. The contributions of CRAND protons to the main peaks increases with energy. Secondary peaks, or bumps in the radial profiles, were caused by more recent solar proton injections that have not yet diffused inward to reach the main peaks. Such injections were directly observed during the last two solar maxima [Hudson *et al.*, 1997; Selesnick *et al.*, 2010]. The gap between main and secondary peaks is a result of the recent solar minimum period, 2007 through 2011, during which there were no significant solar proton events. On average, inward diffusion of CRAND protons is relatively insignificant compared to inward diffusion of solar protons and to the local CRAND source.

Measured energy spectra (Figure 6) also demonstrate the presence of trapped solar protons. For example, at $L = 2.0$ there is a gradual transition from a soft solar proton spectrum for $E \lesssim 40$ MeV to a hard CRAND proton spectrum for $E \gtrsim 40$ MeV. The transition was expected to occur at higher energy, $E \sim 100$ MeV [Selesnick *et al.*, 2007]. Although a consistent feature in the ~ 6 months of data, it occurs in a region where the trapped solar proton intensity depends on relatively recent trapping events and should be variable on a time scale of several years. A lower energy transition at present is therefore unsurprising.

The main peak, near $L = 1.6$ for 26 MeV protons, has a lower intensity than predicted by the model, and it is also lower than earlier measurements from the CRRES satellite [Gusenhoven *et al.*, 1996] by factors ~ 2 to 3. High-energy proton contamination was also an issue for CRRES data. However, though the main peak is formed by CRAND and inward diffusion of solar protons over decades or even centuries, the maximum intensity could have decreased in the 23 years since CRRES. In fact, the model predicts a factor ~ 1.5 decrease since 1991 due to a reduced solar proton source.

As expected, trapped solar protons do not reach the lowest L values ($L \lesssim 1.3$) in any significant number [Jentsch, 1981; Selesnick *et al.*, 2007]. This is demonstrated by the particularly hard CRAND proton spectrum observed at $L = 1.2$ (Figures 5 and 6) and is confirmed by the model simulations (Figures 8–10).

Inner-belt proton intensities for $L \lesssim 3$ did not change significantly during the ~ 6 month interval beginning in October 2013, but for $L \gtrsim 3$ they increased steadily until a sudden decrease on 15 February 2014 for $L > 3.4$ (Figure 7). The changes are consistent with increasing intensity caused by the steady CRAND source [Selesnick *et al.*, 2013] and sudden loss that typically occurs in association with magnetic storms [Selesnick *et al.*, 2010]. However, in this case losses occurred before the only significant storm in near association (February 19) which could therefore not have been causal.

Observed equatorial pitch angle distributions (Figures 3 and 4) show, for $1.8 \lesssim L \lesssim 2.6$, a narrow peak near $\alpha_0 = 90^\circ$ superimposed on a broader shape at lower intensities (a “head-and-shoulders” distribution). Because they are smoothed by the REPT FOV and by the binning in α_0 , this characteristic shape would be enhanced in the actual, unsmoothed distributions (compare unsmoothed and smoothed model distributions, Figures 8 and 9). The model shows that the narrow peak (“head”) is absent from CRAND-only distributions and is therefore formed by trapped solar protons, while the broader shape (“shoulders”) is formed by CRAND protons. In the model, solar protons are trapped with an assumed distribution proportional to $\sin^{12} \alpha_0$. Untrapped solar protons are isotropic, so the trapping process must strongly favor pitch angles near $\alpha_0 = 90^\circ$.

Trapped proton pitch angle distributions at low L are narrow, because of the wide atmospheric loss cones there. They widen with increasing L as the loss cones become narrower. However, for $L \gtrsim 2.2$ the distributions begin to narrow again, both in the data (Figures 3 and 4) and model (Figure 8). This narrowing is caused by trapping limits, the maximum energy of trapped protons as a function of L and α_0 . The limits are lower at higher L , and, for a given L , they are lower at low and high α_0 . Above the trapping limits losses are caused by magnetic field-line-curvature scattering [Young *et al.*, 2008].

The model applies a simple formulation of trapping limits based on adiabatic trapping theory [Selesnick *et al.*, 2013]. It causes all protons above the limit to be immediately lost, forming relatively flat pitch angle distributions at high L . Observations show distributions that are wider but more strongly peaked at $\alpha_0 = 90^\circ$ than are predicted by the model (compare Figures 4 and 9 for $L \gtrsim 2.6$). This suggests that losses associated with the trapping limits are not immediate but diffusive and slow enough to modify the distributions as observed.

The strongly peaked pitch angle distribution of the trapped solar protons means that their intensity at low altitudes ($\lesssim 1000$ km) must be significantly reduced. Observations of inner-belt protons from low-altitude satellites must be dominated by CRAND protons, therefore showing little of the variability caused by solar proton trapping at higher altitudes [Selesnick *et al.*, 2010]. Similarly, the narrow equatorial pitch angle distributions formed by trapping limits for $L \gtrsim 2.6$ mean that low-altitude satellites cannot observe trapped protons at those higher L values. These conclusions are confirmed by low-altitude measurements [Zou *et al.*, 2011].

In summary, observations of equatorial inner-belt protons from REPT, with high resolution in L , E , and α_0 , have revealed details that should provide new constraints on theories for such processes as solar proton trapping, radial diffusion, magnetic storm losses, and losses due to adiabatic trapping limits. They can also be of value in constructing improved empirical and theoretical radiation belt specification models.

Acknowledgments

The authors thank C. A. Kletzing for EMFISIS magnetic field data used in pitch angle determination and M. G. Henderson and G. D. Reeves for magnetic ephemeris data from the IGRF+OP77Q model. Van Allen Probes REPT and ephemeris data are available from the ECT Science Operations and Data Center, <http://www.rbbsp-ect.lanl.gov>, and EMFISIS data from <http://emfisis.physics.uiowa.edu>. This work was supported in part by NASA agreement NNH14AX181 with the Air Force Research Laboratory under the Heliophysics Guest Investigators Program, at University of Colorado and Dartmouth College by RBSP-ECT funding through JHU/APL contract 967399 under prime NASA contract NAS5-01072, and by NSF grant ATM-1023332 to Dartmouth College.

Michael Balikhin thanks Elias Roussos and an anonymous reviewer for their assistance in evaluating this paper.

References

- Baker, D. N., *et al.* (2012), The Relativistic Electron-Proton Telescope (REPT) instrument on board the Radiation Belt Storm Probes (RBSP) spacecraft: Characterization of Earth's radiation belt high-energy particle populations, *Space Sci. Rev.*, **179**, 337–381, doi:10.1007/s11214-012-9950-9.
- Berger, M. J., J. S. Coursey, M. A. Zucker, and J. Chang (2011), Stopping-power and range tables for electrons, protons, and helium ions, NIST, Physical Measurement Laboratory, Gaithersburg, Md. [Available at <http://www.nist.gov/pml/data/star/>].
- Bichsel, H. (1988), Straggling in thin silicon detectors, *Rev. Mod. Phys.*, **60**, 663–699, doi:10.1103/RevModPhys.60.663.
- Chibani, O. (1998), New algorithms for the Vavilov distribution calculation and the corresponding energy loss sampling, *IEEE Trans. Nucl. Sci.*, **45**, 2288–2292, doi:10.1109/23.725266.
- Ginet, G. P., *et al.* (2013), AE9, AP9 and SPM: New models for specifying the trapped energetic particle and space plasma environment, *Space Sci. Rev.*, **179**, 579–615, doi:10.1007/s11214-013-9964-y.
- Gussenhoven, M. S., E. G. Mullen, and D. H. Brautigam (1996), Improved understanding of the Earth's radiation belts from the CRRES satellite, *IEEE Trans. Nucl. Sci.*, **43**(2), 353–368.
- Hudson, M. K., S. R. Elkington, J. G. Lyon, V. A. Marchenko, I. Roth, M. Temerin, J. B. Blake, M. S. Gussenhoven, and J. R. Wygant (1997), Simulations of radiation belt formation during storm sudden commencements, *J. Geophys. Res.*, **102**(A7), 14,087–14,102, doi:10.1029/97JA03995.
- Jentsch, V. (1981), On the role of external and internal source in generating energy and pitch angle distributions of inner-zone protons, *J. Geophys. Res.*, **86**, 701–710, doi:10.1029/JA086iA02p00701.

- Kletzing, C. A., et al. (2013), The Electric and Magnetic Field Instrument Suite and Integrated Science (EMFISIS) on RBSP, *Space Sci. Rev.*, **179**, 127–181, doi:10.1007/s11214-013-9993-6.
- Looper, M. D., J. B. Blake, and R. A. Mewaldt (1998), Maps of hydrogen isotopes at low altitudes in the inner zone from SAMPEX observations, *Adv. Space Res.*, **21**(12), 1679–1682.
- Mauk, B. H., N. J. Fox, S. G. Kanekal, R. L. Kessel, D. G. Sibeck, and A. Ukhorskiy (2012), Science objectives and rationale for the Radiation Belt Storm Probes mission, *Space Sci. Rev.*, **179**, 3–27, doi:10.1007/s11214-012-9908-y.
- Olson, W. P., and K. A. Pfitzer (1977), Magnetospheric magnetic field modeling, *Annual Scientific Report, AFOSR Contract No. F44620-75-C-0033*, McDonnell Douglas Astronautics Co., Huntington Beach, Calif.
- Roederer, J. G. (1970), *Dynamics of Geomagnetically Trapped Radiation*, 166 pp., Springer, New York.
- Sawyer, D. M., and J. I. Vette (1976), AP-8 trapped proton environment for solar maximum and solar minimum, *Tech. Rep., NASA-TM-X-72605, NSSDC/WDC-A-R/S-76-06*, National Aeronautics and Space Administration, Goddard Space Flight Center, Greenbelt, Md.
- Selesnick, R. S. (2014), Optimal performance of charged particle telescopes in space, *Nucl. Instrum. Methods Phys. Res., Sect. A*, **761**, 34–38, doi:10.1016/j.nima.2014.05.109.
- Selesnick, R. S., M. D. Looper, and R. A. Mewaldt (2007), A theoretical model of the inner proton radiation belt, *Space Weather*, **5**, S04003, doi:10.1029/2006SW000275.
- Selesnick, R. S., M. K. Hudson, and B. T. Kress (2010), Injection and loss of inner radiation belt protons during solar proton events and magnetic storms, *J. Geophys. Res.*, **115**, A08211, doi:10.1029/2010JA015247.
- Selesnick, R. S., M. K. Hudson, and B. T. Kress (2013), Direct observation of the CRAND proton radiation belt source, *J. Geophys. Res. Space Physics*, **118**, 7532–7537, doi:10.1002/2013JA019338.
- Vacaresse, A., D. Boscher, S. Bourdarie, M. Blanc, and J. A. Sauvaud (1999), Modeling the high-energy proton belt, *J. Geophys. Res.*, **104**, 28,601–28,613, doi:10.1029/1999JA900411.
- Young, S. L., R. E. Denton, B. J. Anderson, and M. K. Hudson (2008), Magnetic field line curvature induced pitch angle diffusion in the inner magnetosphere, *J. Geophys. Res.*, **113**, A03210, doi:10.1029/2006JA012133.
- Zou, H., Q. G. Zong, G. K. Parks, Z. Y. Pu, H. F. Chen, and L. Xie (2011), Response of high-energy protons of the inner radiation belt to large magnetic storms, *J. Geophys. Res.*, **116**, A10229, doi:10.1029/2011JA016733.

RESEARCH ARTICLE

10.1002/2015JA022154

Key Points:

- Radiation belt protons with $E = 24\text{--}76$ MeV were measured by REPT on Van Allen Probes during 2013–2015
- Increasing intensity at low E near $L = 2$ is consistent with inward diffusion of trapped solar protons
- Low intensity levels at high E near $L = 1.5$ indicate faster than expected loss of CRAND protons

Correspondence to:

R. S. Selesnick,
richard.selesnick@us.af.mil

Citation:

Selesnick, R. S., D. N. Baker, A. N. Jaynes, X. Li, S. G. Kanekal, M. K. Hudson, and B. T. Kress (2016), Inward diffusion and loss of radiation belt protons, *J. Geophys. Res. Space Physics*, 121, doi:10.1002/2015JA022154.

Received 10 NOV 2015

Accepted 8 FEB 2016

Accepted article online 10 FEB 2016

Inward diffusion and loss of radiation belt protons

R. S. Selesnick¹, D. N. Baker², A. N. Jaynes², X. Li^{2,3}, S. G. Kanekal⁴, M. K. Hudson⁵, and B. T. Kress^{6,7}
¹Space Vehicles Directorate, Air Force Research Laboratory, Kirtland AFB, New Mexico, USA, ²Laboratory for Atmospheric and Space Physics, University of Colorado Boulder, Boulder, Colorado, USA, ³Department of Aerospace Engineering Sciences, University of Colorado Boulder, Boulder, Colorado, USA, ⁴NASA Goddard Space Flight Center, Greenbelt, Maryland, USA, ⁵Department of Physics and Astronomy, Dartmouth College, Hanover, New Hampshire, USA, ⁶Center for Cooperative Research in the Environmental Sciences, University of Colorado Boulder, Boulder, Colorado, USA, ⁷National Center for Environmental Information, NOAA, Boulder, Colorado, USA

Abstract Radiation belt protons in the kinetic energy range 24 to 76 MeV are being measured by the Relativistic Electron Proton Telescope on each of the two Van Allen Probes. Data have been processed for the purpose of studying variability in the trapped proton intensity during October 2013 to August 2015. For the lower energies ($\lesssim 32$ MeV), equatorial proton intensity near $L = 2$ showed a steady increase that is consistent with inward diffusion of trapped solar protons, as shown by positive radial gradients in phase space density at fixed values of the first two adiabatic invariants. It is postulated that these protons were trapped with enhanced efficiency during the 7 March 2012 solar proton event. A model that includes radial diffusion, along with known trapped proton source and loss processes, shows that the observed average rate of increase near $L = 2$ is predicted by the same model diffusion coefficient that is required to form the entire proton radiation belt, down to low L , over an extended ($\sim 10^3$ year) interval. A slower intensity decrease for lower energies near $L = 1.5$ may also be caused by inward diffusion, though it is faster than predicted by the model. Higher-energy ($\gtrsim 40$ MeV) protons near the $L = 1.5$ intensity maximum are from cosmic ray albedo neutron decay. Their observed intensity is lower than expected by a factor ~ 2 , but the discrepancy is resolved by adding an unspecified loss process to the model with a mean lifetime ~ 120 years.

1. Introduction

Radiation belt protons originate from cosmic ray albedo neutron decay (CRAND) and from trapping of solar protons [Selesnick *et al.*, 2007]. The steady CRAND source combines with slow inward diffusion of solar protons to create a relatively stable inner belt ($L \lesssim 1.7$) [Albert *et al.*, 1998]. Farther out ($L \gtrsim 2.3$), more rapid changes are caused by storm time loss and by trapping during solar proton events [Selesnick *et al.*, 2010]. The intermediate region typically exhibits gradual change on time scales ~ 1 year [Albert and Ginat, 1998].

Trapped protons are now being measured by the Relativistic Electron Proton Telescope (REPT) on each of the two Van Allen Probes [Baker *et al.*, 2012]. The pulse-height-analyzed (PHA) data, available at a sufficiently high rate since October 2013, have already provided a detailed description of the stable population during late 2013 and early 2014 [Selesnick *et al.*, 2014]. Substantially, more data are now available, providing an opportunity to study variability up to late 2015.

Quantitative interpretation of the measured trapped proton distribution, as a function of location, energy, and time, requires modeling of combined source, loss, and transport processes [Selesnick *et al.*, 2007, 2013]. Some aspects, such as the radial diffusion coefficient and solar proton trapping efficiency, presently are not well determined by theory or measurement. Comparison of model results to the REPT data can provide new or improved constraints.

This work aims to describe both the new results from REPT and their interpretation based on updated modeling. The data analysis (section 2) leads to proton equatorial perpendicular intensity and to phase space density as a function of the three adiabatic invariants of trapped particle motion. Modeling results are compared to both representations of the data (section 3), leading to several conclusions about required source, loss, and transport coefficients (section 4).

2. Data Analysis

Analysis of the PHA proton data from REPT, for computation of equatorial intensity, has been described in detail previously [Selesnick *et al.*, 2014], and only a brief summary is given here. A new method for computation of phase space density is also described.

2.1. Equatorial Intensity

Each REPT consists of a series of nine aligned Si detectors. The PHA data provide a set of “events,” each containing the energy loss measurement from each detector resulting from a single particle. The REPT geometry factor is well defined for protons that enter through the collimated (32° full angle) aperture, pass through one or more detectors, and stop in the subsequent detector, enabling accurate normalization of particle flux. Their kinetic energy prior to entering REPT is in the range ~24 to 76 MeV. A reduced data set containing only such proton events (referred to as “valid”) is created by eliminating all events from protons outside this range and from other particle types (predominantly electrons).

After valid proton events have been identified, the reduced data set is used to compute equatorial differential unidirectional proton intensity j_0 by binning events in time t , kinetic energy E , equatorial pitch angle α_0 , and L shell. It is related to the number of valid events N in each multidimensional bin, defined by chosen intervals Δt centered at t , ΔE at E , $\Delta \alpha_0$ at α_0 , and ΔL at L :

$$j_0(t, E, \alpha_0, L) = \frac{\delta t}{\epsilon G \Delta t \Delta E} \sum_{i=1}^N r_i \quad (1)$$

where $G = 0.2 \text{ cm}^2 \text{ sr}$ is the REPT geometry factor and $\epsilon = 1$ is the proton detection efficiency (scattering effects, which could marginally reduce ϵ , are neglected). The summation is over all valid events within the bin. Each event is weighted, as shown, by the concurrent counting rate r_i of the front detector, which initiates event analysis, because only a single event is analyzed during each time step of length $\delta t = 12 \text{ ms}$. This method accounts, on average, for those protons that were not recorded as PHA events during each δt .

Local pitch angles of the REPT axis are determined from field directions measured by the EMFIS (Electric and Magnetic Field Instrument Suite and Integrated Science) magnetometer [Kletzing *et al.*, 2013]. They are converted to equatorial pitch angles α_0 using model local and equatorial magnetic field magnitudes calculated from IGRF (International Geomagnetic Reference Field) [Thébault *et al.*, 2015] combined with OP77Q (Olson-Pfizer 1977 Quiet) [Olson and Pfizer, 1977]. Values of L (defined in section 2.2) are from the same magnetic field models.

Equatorial perpendicular intensity is shown as a function of L , for five separate energy ranges, in Figure 1. It was computed from equation (1) by including data from both REPT-A and REPT-B (i.e., from both Van Allen Probes), α_0 values of $90 \pm 15^\circ$ ($\Delta \alpha_0 = 30^\circ$), and with a resolution in L of $\Delta L = 0.05$. Monthly averages are shown (though $\Delta t < 1$ month, depending on orbital coverage for each L and α_0 bin) for November 2013 (solid curves) and July 2015 (dashed curves), illustrating intensity changes as a function of L over a period of 21 months.

The most significant changes were seen for the lower energy range, 24 to 28 MeV. A closer view of the high-intensity region, for this range only but including all monthly averages from October 2013 to August 2015, is shown in Figure 2. This represents the full 23 month analyzed data set. Changes are seen to occur smoothly on the monthly time scale. This is illustrated further in Figure 3; intensity values at $L = 1.5$ (left) and $L = 1.9$ (right), near local maxima as a function of L identified from the previous figures, are shown as a function of time for all five energy ranges and with the same monthly time resolution. Although the variations are smooth as already noted, within statistical uncertainties, they do not occur at a perfectly steady rate.

Results have been shown from a combination of REPT-A and REPT-B, effectively averaging over the two spacecraft. In fact, intensities computed from REPT-A alone are typically ~10% higher than from REPT-B alone, for presently unknown reasons. This introduces ~10% systematic uncertainty into the results, in addition to the statistical errors illustrated in Figure 3, but has little effect on any other conclusions of the study.

2.2. Phase Space Density

Radiation belt transport is usually described by a diffusion equation for the phase space density f , resulting from violation of one or more adiabatic invariants [Schulz and Lanzerotti, 1974]. For data interpretation

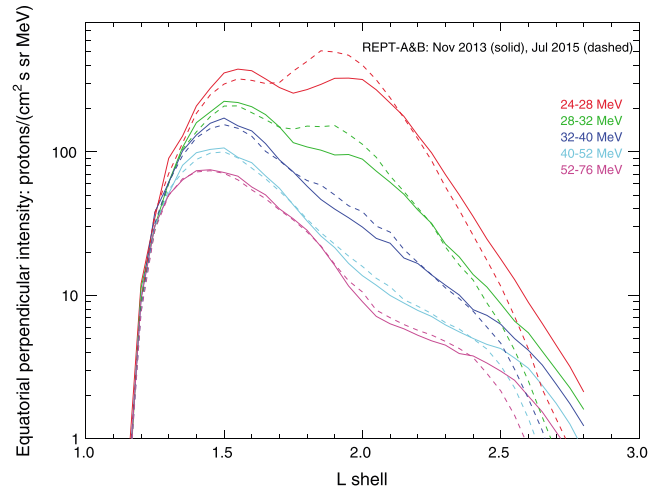


Figure 1. Equatorial perpendicular differential proton intensity versus L , measured by REPT-A and REPT-B, color coded by the indicated energy ranges. Monthly averages are included from November 2013 (solid curves) and July 2015 (dashed curves). Data are also averaged over the equatorial pitch angle range $75^\circ < \alpha_0 < 105^\circ$ and over L intervals of 0.05.

it is therefore useful to determine f as a function of the three adiabatic invariants, M , K , and L [Roederer, 1970]:

$$M = \frac{p^2}{2m_p B_m} \quad (2)$$

$$K = \int_{s_m}^{s'_m} \sqrt{B_m - B(s)} ds \quad (3)$$

$$L = \frac{2\pi k_0}{R_E \Phi} \quad (4)$$

where p is momentum, m_p is the proton mass, B is local magnetic field, B_m is mirror magnetic field, s is distance along a field line between mirror points s_m and s'_m , Φ is the magnetic flux enclosed by a drift shell, k_0 is Earth's dipole moment, and $R_E = 6371.2$ km is Earth's radius. For this work the invariant L is replaced by L_m , the McIlwain L shell [Roederer, 1970], defined with the dipole moment of date (and already used in Figures 1–3), as they differ negligibly for $L < 3.5$. All three adiabatic invariants can be computed with relatively high accuracy

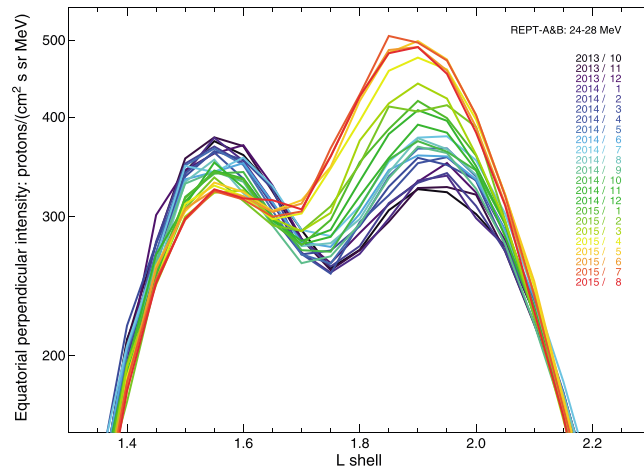


Figure 2. Similar to Figure 1 but for only the lowest-energy range, 24 to 28 MeV, including all monthly averages from October 2013 to August 2015 (color coded by year/month), and with a change of scale.

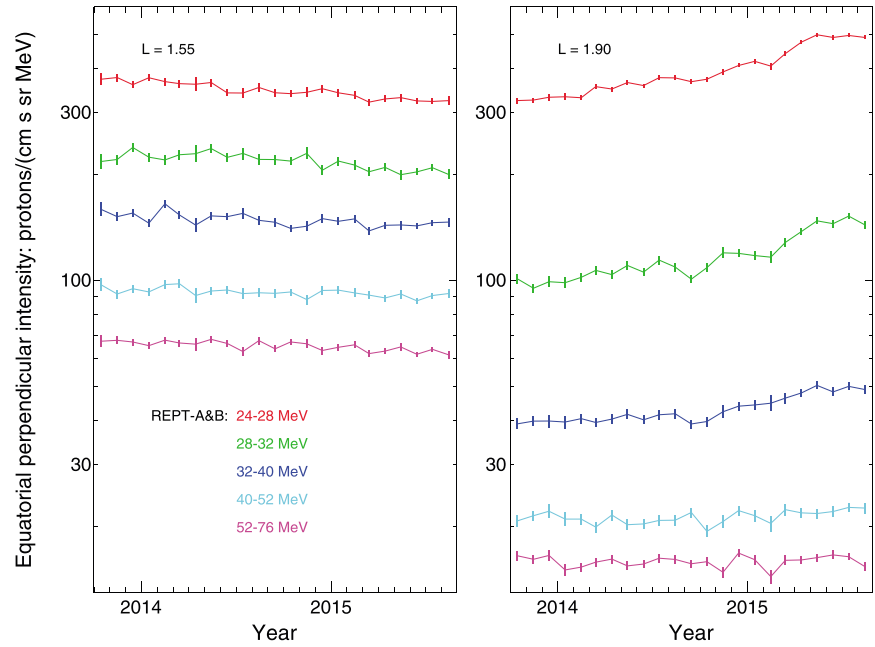


Figure 3. Monthly averaged equatorial perpendicular differential proton intensity versus time, from October 2013 to August 2015, measured by REPT-A and REPT-B, for (left) $L = 1.55$ and (right) $L = 1.90$, color coded by the indicated energy ranges (applicable to both sides). Statistical 1σ error bars are included. Ranges of E , α_0 , and L are as in Figure 1.

at low L because the magnetic field there is dominated by the internal IGRF field model, which is more accurate than the external field models that cause significant error at higher L . Computed phase space densities are therefore expected to be relatively accurate at low L .

Phase space density f is related to local directional intensity j by $f = j/p^2$. To compute f , the reduced event data are binned in t , M , K , and L :

$$f(t, M, K, L) = \frac{\delta t}{\epsilon G \Delta t} \sum_{i=1}^N \frac{r_i}{p_i^2 \Delta E_i} \quad (5)$$

where momentum p_i and energy range ΔE_i are evaluated at the energy E and mirror field B_m of each proton event i and so are included in the summation (although average values for each bin could equally be used). Comparing to equation (1), N is now the number of protons in each new multidimensional bin, defined by Δt centered at t , ΔM at M , ΔK at K , and ΔL at L . Other quantities are as in equation (1). The change of variables to M and K gives (for nonrelativistic protons)

$$\Delta E_i = \frac{\partial E}{\partial M} \Delta M + \frac{\partial E}{\partial K} \Delta K = B_m \Delta M + \frac{2M\sqrt{B_m}}{S_b} \Delta K \quad (6)$$

where the path length between mirror points is [Roederer, 1970]

$$S_b = \int_{s_m}^{s'_m} \frac{ds}{\sqrt{1 - \frac{B(s)}{B_m}}} \quad (7)$$

Phase space density, computed from (5), is shown versus L in Figure 4, for the same two time intervals as in Figure 1. Two K intervals (computed for the REPT look direction) are included, corresponding to nearly equatorially mirroring protons (Figure 4, top) and to protons mirroring at midlatitudes (Figure 4, bottom). Various M intervals are selected for each case, and results for each one cover L ranges corresponding to the energy range of the data, ~ 24 to 76 MeV (high to low L). The M and K intervals are wide enough that statistical errors are small, at high phase space density, as shown in the figure by low levels of fluctuation.

Radial gradients of f show the direction of diffusive flow, which is outward in regions of negative gradient and inward in regions of positive gradient. In particular, large positive gradients are observed near $L = 2$ for the lower energy protons (outer part of the L range covered by any given M interval) with lower K values. Therefore, inward diffusion might account for the increasing intensity observed there (Figures 1–3). This can be verified by modeling, as described in the next section.

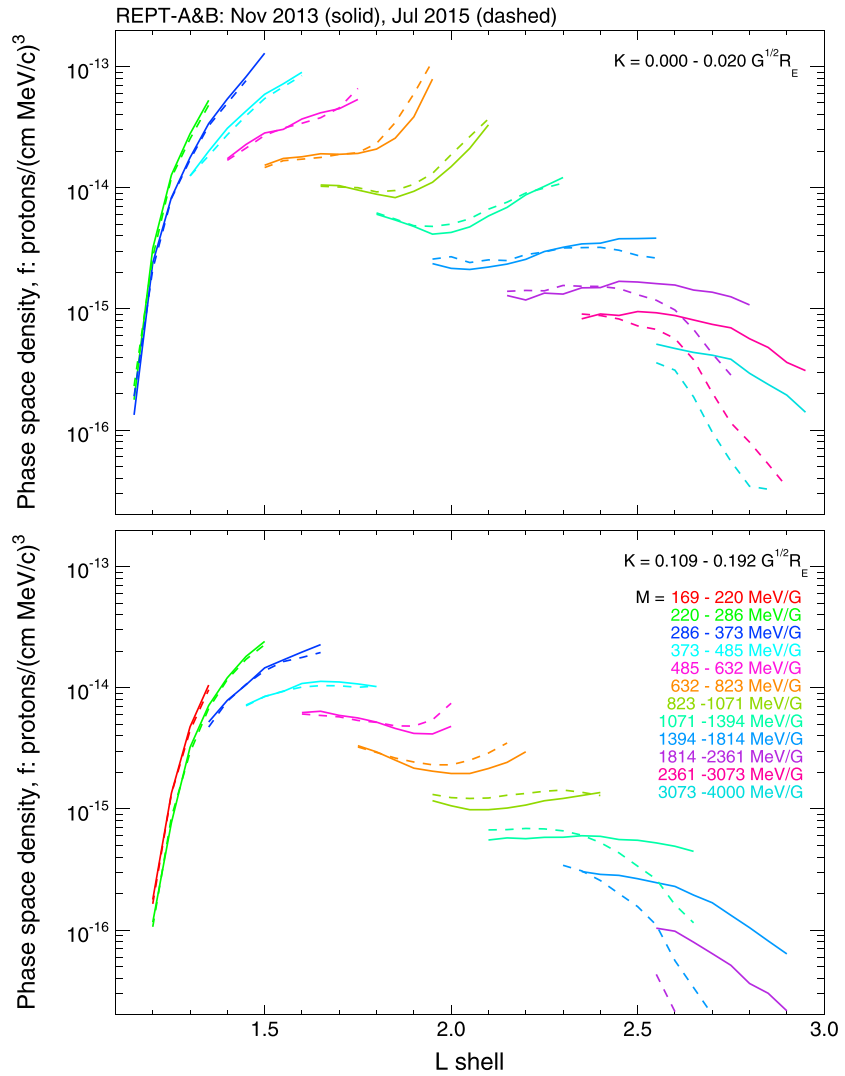


Figure 4. Phase space density versus L for the indicated fixed ranges of the first and second adiabatic invariants, M and K , measured by REPT-A and REPT-B. Monthly averages are included from November 2013 (solid curves) and July 2015 (dashed curves). Ranges of K correspond to (top) near-equatorially mirroring protons and (bottom) protons mirroring at midlatitudes. Color coding by M applies to both K ranges.

3. Model

Source and loss processes governing the proton distribution near the heart of the inner radiation belt, $L \sim 1.5$, occur over long time scales. Time scales are shorter at lower and higher L , where intensities typically are lower as a result. Modeling the entire belt can start from an initial condition (such as the solid curves in Figure 1) and proceed to later times (as represented by the dashed curves). Then the creation of the initial state, which depends on the slow processes, is not addressed, and only those processes that change the belt from the initial to final state need be included. An alternative is to model all processes that form the radiation belt from early times and determine whether all observed states of the radiation belt (solid and dashed curves) are reproduced. The latter approach is followed in this work, because it provides greater insight into the slow processes that produce the radiation belt and because an appropriate model is available.

The model has been described in detail previously [Selesnick *et al.*, 2007, 2013, 2014], and only a brief summary is given here, with emphasis on aspects relevant to this work. Phase space density of trapped protons at time t is computed as the expected value \mathcal{E} over a set of path integrals:

$$f(t) = \mathcal{E} \left(\int_{t_0}^t \frac{S(t')}{p^2(t')} \exp \left[- \int_{t'}^t \frac{dt''}{\tau(t'')} \right] dt' \right) \quad (8)$$

Approved for public release; distribution is unlimited.

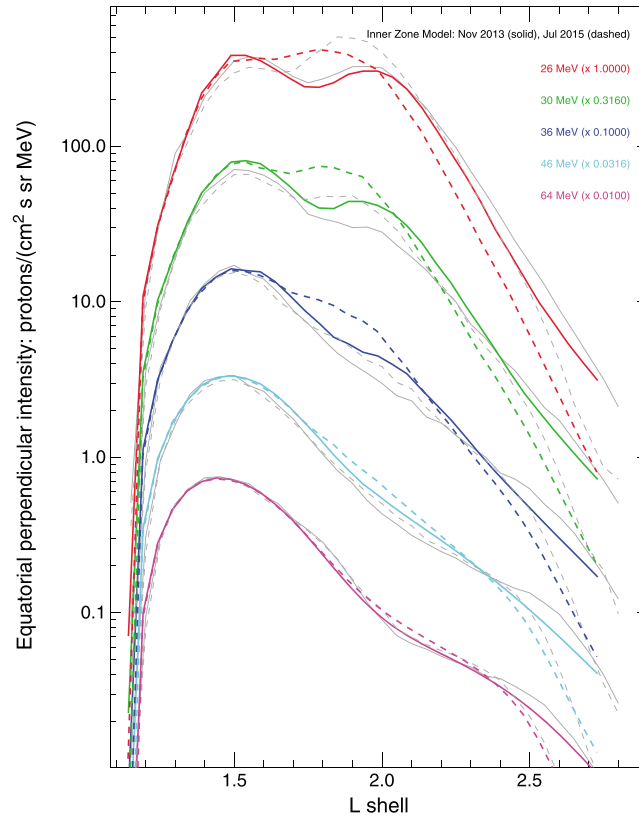


Figure 5. Model equatorial perpendicular differential proton intensity versus L , color coded by energy and multiplied by the listed factors for clarity. The model was evaluated for 15 November 2013 (solid curves) and 15 July 2015 (dashed curves). For comparison, the data curves from Figure 1 are also shown (here in gray), multiplied by the same factors.

where S is the net CRAND and solar proton source (or trapped intensity production rate) and τ is the net mean lifetime;

$$\frac{1}{\tau} = \frac{1}{\gamma p} \frac{\partial}{\partial E} \left(\gamma p \frac{dE}{dt} \right) + \frac{1}{\tau_n} + \frac{1}{\tau_s} + \frac{1}{\tau_a} \quad (9)$$

where dE/dt is the energy loss rate, of protons with momentum p and Lorentz factor γ , to the neutral atmosphere and ionosphere/plasmasphere, τ_n is lifetime for steady loss by inelastic nuclear scattering, τ_s is for episodic loss during magnetic storms, and τ_a accounts for any required additional loss as described below. The initial time t_0 is early enough for S to produce the entire belt, and for any initial condition to have decayed away, by the time t .

Proton paths in E and L are computed by simultaneously integrating dE/dt and the stochastic differential equation for radial diffusion [Selesnick, 2012]:

$$dL = -L^2 \frac{\partial}{\partial L} \left(\frac{D_{LL}}{L^2} \right) dt + \sqrt{2D_{LL}} dW \quad (10)$$

where D_{LL} is the diffusion coefficient and dW is a standard Brownian motion (or Wiener process). Diffusion is assumed to be the only radial transport mechanism. After each step dL in L , E is changed to conserve M and K and additionally by the energy loss from dE/dt during the time step dt . Many paths are computed backward in time by Monte Carlo simulation from a given final location, and as represented by the expectation \mathcal{E} in equation (8), integrals along each path are averaged to obtain f .

Model proton intensity near $L = 1.5$ was previously found to be higher than obtained from REPT data taken during early 2014, by factors ~ 2 [Selesnick et al., 2014]. However, the model includes several parameters that

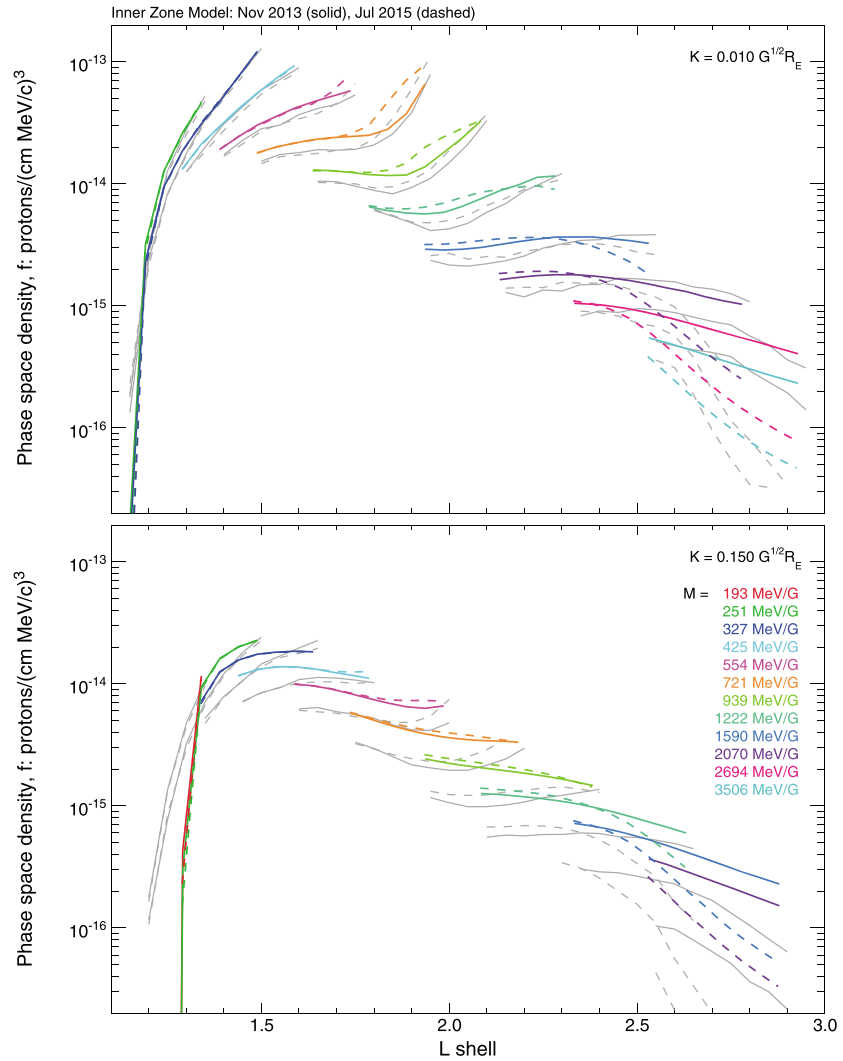


Figure 6. Model phase space density versus L for the indicated fixed values of the first and second adiabatic invariants, M and K . The model was evaluated for 15 November 2013 (solid curves) and 15 July 2015 (dashed curves). Values of K correspond to (top) near-equatorially mirroring protons and (bottom) protons mirroring at midlatitudes. Color coding by M applies to both K values. For comparison, the data curves from Figure 4 are also shown (here in gray).

can be adjusted for a better fit. This has been done, as described below, to improve the fit to the earlier measurements in Figure 1, from November 2013, and results are shown in Figure 5 (solid curves, color coded by energy). The same model was run for the time of the later measurements shown in Figure 1, July 2015, and those results are also shown in Figure 5 (colored dashed curves), as are data from Figure 1 for comparison (gray curves). Model phase space density at constant M and K , for the same two times, is shown versus L in Figure 6, where data from Figure 4 are also shown for comparison. In all cases the model was computed for times, energies and pitch angles, or M and K values, at the center of each data bin.

Required changes to model parameters, for improving the fit to the early REPT data, are not necessarily unique, and some possible alternatives are discussed in section 4. However, the chosen adjustments bring the model results closer to the data and are described here:

1. To reduce the intensity of trapped solar protons, the trapping time scale, which is inversely related to trapping efficiency [Selesnick *et al.*, 2007], was increased to

$$\tau_p = 300 \left(\frac{E}{1 \text{ MeV}} \right)^{\frac{5}{2}} \text{ s} \quad (11)$$

2. To supply sufficient solar protons to low L , as a function of energy, the radial diffusion coefficient was modified to

$$D_{LL} = 6 \times 10^{-11} L^9 \left(\frac{1 \text{ MeV}}{E} \right)^{\frac{3}{2}} \left(\frac{k_0}{0.3 GR_E^3} \right)^{\frac{16}{3}} s^{-1} \quad (12)$$

The dependence on Earth's dipole moment k_0 , previously neglected, is appropriate to radial diffusion caused by magnetic impulses [Schulz, 1975] (a similar dependence applies to electrostatic impulses). Time-dependent values of k_0 since 1900 are determined by IGRF and prior to 1900 by CALS7K (Continuous Archeomagnetic and Lake Sediment, 7k years model) [Korte and Constable, 2005] (as shown in Figure 1 of Selesnick *et al.* [2007]).

3. To reduce the intensity of trapped protons from CRAND, additional loss was included with mean lifetime

$$\tau_a = 8.64 \times 10^9 L^{-2} s \quad (13)$$

(or $10^5 L^{-2}$ days). This corresponds to a mean lifetime at $L = 1.5$ of 122 years. (By comparison, energy loss and scattering time scales in equation 9 are respectively ~ 10 and 50 times longer for equatorial 64 MeV protons at $L = 1.5$.) Previous versions of the model had no additional loss.

4. To increase the local intensity maximum near $L = 2$, which was created by solar proton trapping during recent years, the energy spectrum of the largest recent solar proton event, on 7 March 2012, was modified from the average double power law type spectrum used for all other events [Selesnick *et al.*, 2007]. The fluence spectrum $F(E)$ used for the event was a single power law:

$$F = 2.2 \times 10^{17} \left(\frac{E}{1 \text{ MeV}} \right)^{-8} (\text{cm}^2 \text{ sr MeV})^{-1} \text{ for } E > 10 \text{ MeV} \quad (14)$$

and $F = 0$ for $E < 10$ MeV. This change has the effect of increasing the trapped proton intensity from this event for the lower observed energies.

4. Discussion and Conclusions

Proton intensity has been derived for equatorial pitch angles near $\alpha_0 = 90^\circ$ because the local intensity maximum near $L = 2$ is most prominent in that case, as shown by comparison to omnidirectional results [Selesnick *et al.*, 2014, Figure 5]. The changing intensity near $L = 2$ during 2014 and 2015 (Figures 1–3) is consistent with inward diffusion of trapped solar protons. This conclusion is supported by large positive radial gradients in observed phase space density for low K (Figure 4). Modeling shows that such gradients could have been formed by enhanced trapping efficiency during the 7 March 2012 solar proton event, although, because it occurred before the launch of Van Allen Probes, it is possible that another event, or some combination of events, was responsible. Proton trapping has been directly observed on several occasions [Selesnick *et al.*, 2010], with a particularly significant event occurring in March 1991 [Mullen *et al.*, 1991].

The energy spectrum of solar protons immediately after trapping is the main factor that later determines, for various observed energies, both intensity gradients for $L > 2$ and locations of intensity maxima near $L = 2$. It was not possible to match all of these features in the data with a simple model of the injected spectrum, and it is likely that better agreement could be achieved with a more detailed model. However, the general characteristics of increasing intensity near the maxima, and slow inward transport of the maxima, were evident in the model, in near-quantitative agreement with observations (Figure 5). This was achieved with the same model radial diffusion coefficient D_{LL} , including time, L , and energy dependences (equation (12)), that produced the stable belt at lower L over a much longer interval ($\sim 10^3$ years). However, variations in the observed rate of intensity change near $L = 2$ suggests that D_{LL} varies on those time scales (\sim months) and that the model D_{LL} represents a longer-term average.

Compared to earlier estimates of D_{LL} also based on proton radiation belt modeling [Farley *et al.*, 1970; Jentsch, 1981; Albert *et al.*, 1998], the value derived here has similar or identical L dependence, though the magnitudes of earlier estimates were somewhat lower (by factors ~ 2 to 10, depending on time and energy), perhaps because of the inclusion here of an additional loss process. It might be possible to obtain more accurate estimates of recent D_{LL} values by modeling only the recent evolution of the belt, starting from an initial condition based on the early REPT data. However, extrapolation of the observed proton distribution outside the REPT energy range would be required to fully specify the required initial condition, introducing some uncertainty.

Phase space density results are also consistent with the conclusion that the intensity maximum near $L = 2$ is produced by inward diffusion only of the near-equatorial protons, because a large positive radial gradient is not observed at higher K . The model was not optimized for higher K protons, and so the fit to the data is less accurate in that case (Figure 6). Also, the range of K values included in the data used for computing phase space density means that the model, computed for a single K , is not directly comparable, particularly for the lowest L values. (For example, protons at $L = 1.2$ are inside the atmospheric loss cone for $K \gtrsim 0.05 \text{ G}^{1/2} R_E$ and no trapped protons are expected for $K = 0.15 \text{ G}^{1/2} R_E$, as shown by the model; for $L = 1.6$ the loss cone is $K \gtrsim 0.5 \text{ G}^{1/2} R_E$ and $K = 0.15 \text{ G}^{1/2} R_E$ corresponds, at 0° longitude, to $\alpha_0 \approx 56^\circ$.)

The local intensity maximum near $L = 1.5$ showed, at the lower observed energies, a slow but steady decrease during 2014 and 2015 (Figures 1–3). The model intensity also decreased, due to inward diffusion, but by a lesser amount. Compared to the observed intensity increase near $L = 2$, it is less clear that the decrease near $L = 1.5$ is consistent with radial diffusion alone, or whether some unknown process is primarily responsible.

Alternatives to radial diffusion, to explain the decreasing intensity near $L = 1.5$, are a decrease in the source strength S , an increase in the energy loss rate dE/dt , or decrease in the lifetime τ . All of these factors are time dependent in the model, through a parameterization by solar radio flux ($F_{10.7}$) which varies with solar cycle phase. The primary effect is on dE/dt , due to changing atmospheric density. During the present declining phase of the solar cycle the density is expected to be decreasing and, therefore, the trapped proton intensity increasing at low altitude [Selesnick et al., 2007], opposite to the observed changes. At higher altitudes the time dependence is reduced and there is a phase lag relative to the solar cycle, but the effect is negligible for equatorial protons near $L = 1.5$, as shown by the model results, and a convincing explanation for the decreasing intensity observed there at lower energies remains elusive.

To fit observed intensities at higher energies, it was necessary to include additional loss in the model of unknown origin (equation (13)). This lowers the model intensity, for $E = 64 \text{ MeV}$ near $L = 1.5$, by a factor ~ 2 . A similar reduction could be achieved by lowering the CRAND source. It was computed by Monte Carlo simulation of albedo neutron production [Selesnick et al., 2007] and could be in error. However, the source strength was verified by observations of trapped proton replenishment following magnetic storm loss [Selesnick et al., 2013]. Also, a reduction in the CRAND source would apply equally at all L , rather than just at low L as required (the additional loss is effective only at low L because of the otherwise much longer lifetimes there). Therefore, an additional loss process appears to be the most likely explanation of the observed intensity levels at higher energies.

A candidate for the additional loss process is elastic nuclear (Coulomb) scattering from the neutral atmosphere and ambient plasma. However, this was shown previously to have only a minor influence on trapped proton intensity [Selesnick et al., 2008]. In fact, the scattering lifetime at $L = 1.5$ is $\sim 10^5$ years [Albert et al., 1998], much longer than the required value of ~ 120 years. Also, scattering rates would be higher at lower L , rather than the inverse as required by the data. A more likely candidate is scattering by shear Alfvén waves [Dragt, 1961; Shao et al., 2009] or, more generally, electromagnetic ion cyclotron (EMIC) waves [de Soria-Santacruz et al., 2013]. Measured distributions of H^+ or He^+ band EMIC waves [Saikin et al., 2015], extrapolated to lower L , may provide the necessary low average wave power. Such scattering would modify the trapped proton distribution in α_0 (or K), which could be modeled as pitch angle diffusion by an equation analogous to (10). However, there are presently no estimates of the appropriate diffusion coefficient.

Finally, measurements for $L \gtrsim 2.4$ show a significant decrease in trapped proton intensity during 2015. It was coincident with the magnetic storm of 17 March (and perhaps also the storm of 23 June). Loss during magnetic storms is included in the model, based on an empirical lifetime that depends on L and the minimum storm time Dst [Selesnick et al., 2013], and is modified by subsequent radial diffusion. Model results (Figure 5) show close agreement with the data in the extent and depth of the loss, at least for the higher proton energies.

References

- Albert, J. M., and G. P. Ginat (1998), CRRES observations of radiation belt protons 2. Time-dependent radial diffusion, *J. Geophys. Res.*, **103**, 14,865–14,877, doi:10.1029/97JA00290.
- Albert, J. M., G. P. Ginat, and M. S. Gussenhoven (1998), CRRES observations of radiation belt protons 1. Data overview and steady state radial diffusion, *J. Geophys. Res.*, **103**, 9261–9274, doi:10.1029/97JA02869.
- Baker, D. N., et al. (2012), The Relativistic Electron-Proton Telescope (REPT) instrument on board the Radiation Belt Storm Probes (RBSP) spacecraft: Characterization of Earth's radiation belt high-energy particle populations, *Space Sci. Rev.*, **179**, 337–381, doi:10.1007/s11214-012-9950-9.

Acknowledgments

Van Allen Probes REPT and ephemeris data are available from the ECT Science Operations and Data Center, <http://www.rbsp-ect.lanl.gov>; EMFISIS data are available from <http://emfisis.physics.uiowa.edu>. We thank T.P. O'Brien for pointing out the work of Schulz [1975]. This work was supported in part by NASA agreement NNH14AX18I with the Air Force Research Laboratory under the Heliophysics Guest Investigators Program, at University of Colorado and Dartmouth College by RBSP-ECT funding through JHU/APL contract 967399 under prime NASA contract NAS5-01072, and, at Dartmouth College, by NASA grant NNX15AF54G and National Science Foundation grant AGS-1455470.

- de Soria-Santacruz, M., K. G. Orlova, M. Martinez-Sanchez, and Y. Y. Shprits (2013), Scattering rates of inner belt protons by EMIC waves: A comparison between test particle and diffusion simulations, *Geophys. Res. Lett.*, **40**, 4793–4797, doi:10.1002/grl.50925.
- Dragt, A. J. (1961), Effect of hydromagnetic waves on the lifetime of Van Allen radiation protons, *J. Geophys. Res.*, **66**(6), 1641–1649, doi:10.1029/JZ066i006p01641.
- Farley, T. A., A. D. Tomassian, and M. Walt (1970), Source of high-energy protons in the Van Allen radiation belt, *Phys. Rev. Lett.*, **25**(1), 47–49.
- Jentsch, V. (1981), On the role of external and internal source in generating energy and pitch angle distributions of inner-zone protons, *J. Geophys. Res.*, **86**, 701–710.
- Kletzing, C. A., et al. (2013), The Electric and Magnetic Field Instrument Suite and Integrated Science (EMFISIS) on RBSP, *Space Sci. Rev.*, **179**, 127–181, doi:10.1007/s11214-013-9993-6.
- Korte, M., and C. G. Constable (2005), Continuous geomagnetic field models for the past 7 millennia: 2. CALS7K, *Geochem. Geophys. Geosyst.*, **6**, Q02H16, doi:10.1029/2004GC000801.
- Mullen, E. G., M. S. Gussenhoven, K. Ray, and M. Violet (1991), A double-peaked inner radiation belt: Cause and effect as seen on CRRES, *IEEE Trans. Nucl. Sci.*, **38**(6), 1713–1718, doi:10.1109/23.124167.
- Olson, W. P., and K. A. Pfitzer (1977), Magnetospheric magnetic field modeling, *Annu. Sci. Rep., AFOSR Contract No. F44620-75-C-0033*, McDonnell Douglas Astronautics, Huntington Beach, Calif.
- Roederer, J. G. (1970), *Dynamics of Geomagnetically Trapped Radiation*, 166 pp., Springer, New York.
- Saikin, A. A., J.-C. Zhang, R. C. Allen, C. W. Smith, L. M. Kistler, H. E. Spence, R. B. Torbert, C. A. Kletzing, and V. K. Jordanova (2015), The occurrence and wave properties of H⁺-, He⁺-, and O⁺-band EMIC waves observed by the Van Allen Probes, *J. Geophys. Res. Space Physics*, **120**, 7477–7492, doi:10.1002/2015JA021358.
- Schulz, M. (1975), Paleomagnetospheric radial diffusion, *Geophys. Res. Lett.*, **2**, 173–175, doi:10.1029/GL002i005p00173.
- Schulz, M., and L. J. Lanzerotti (1974), *Particle Diffusion in the Radiation Belts*, 216 pp., Springer, New York.
- Selesnick, R. S. (2012), Atmospheric scattering and decay of inner radiation belt electrons, *J. Geophys. Res.*, **117**, A08218, doi:10.1029/2012JA017793.
- Selesnick, R. S., M. D. Looper, and R. A. Mewaldt (2007), A theoretical model of the inner proton radiation belt, *Space Weather*, **5**, S04003, doi:10.1029/2006SW000275.
- Selesnick, R. S., M. D. Looper, and R. A. Mewaldt (2008), A model of the secondary radiation belt, *J. Geophys. Res.*, **113**, A11221, doi:10.1029/2008JA013593.
- Selesnick, R. S., M. K. Hudson, and B. T. Kress (2010), Injection and loss of inner radiation belt protons during solar proton events and magnetic storms, *J. Geophys. Res.*, **115**, A08211, doi:10.1029/2010JA015247.
- Selesnick, R. S., M. K. Hudson, and B. T. Kress (2013), Direct observation of the CRAND proton radiation belt source, *J. Geophys. Res. Space Physics*, **118**, 7532–7537, doi:10.1002/2013JA019338.
- Selesnick, R. S., D. N. Baker, A. N. Jaynes, X. Li, S. G. Kanekal, M. K. Hudson, and B. T. Kress (2014), Observations of the inner radiation belt: CRAND and trapped solar protons, *J. Geophys. Res. Space Physics*, **119**, 6541–6552, doi:10.1002/2014JA020188.
- Shao, X., K. Papadopoulos, and A. S. Sharma (2009), Control of the energetic proton flux in the inner radiation belt by artificial means, *J. Geophys. Res.*, **114**, A07214, doi:10.1029/2009JA014066.
- Thébault, E., et al. (2015), International geomagnetic reference field—The twelfth generation, *Earth Planets Space*, **67**, 79, doi:10.1186/s40623-015-0228-9.

DISTRIBUTION LIST

DTIC/OCP

8725 John J. Kingman Rd, Suite 0944

Ft Belvoir, VA 22060-6218 1 cy

AFRL/RVIL

Kirtland AFB, NM 87117-5776 2 cys

Official Record Copy

AFRL/RVBXR/Dr. Richard Selesnick 1 cy

This page is intentionally left blank.